11-8

SANDIA REPORT

SAND95–2342 • UC–703
Unlimited Release
Printed October 1995

Experimental Measurements of the Hugoniot of Stishovite

Michael D. Furnish, Eichi Ito

Prepared by
Sandia National Laboratories
Albuquerque, New Mexico 87185 and Livermore, California 94550
for the United States Department of Energy
under Contract DE-AC04-94AL85000

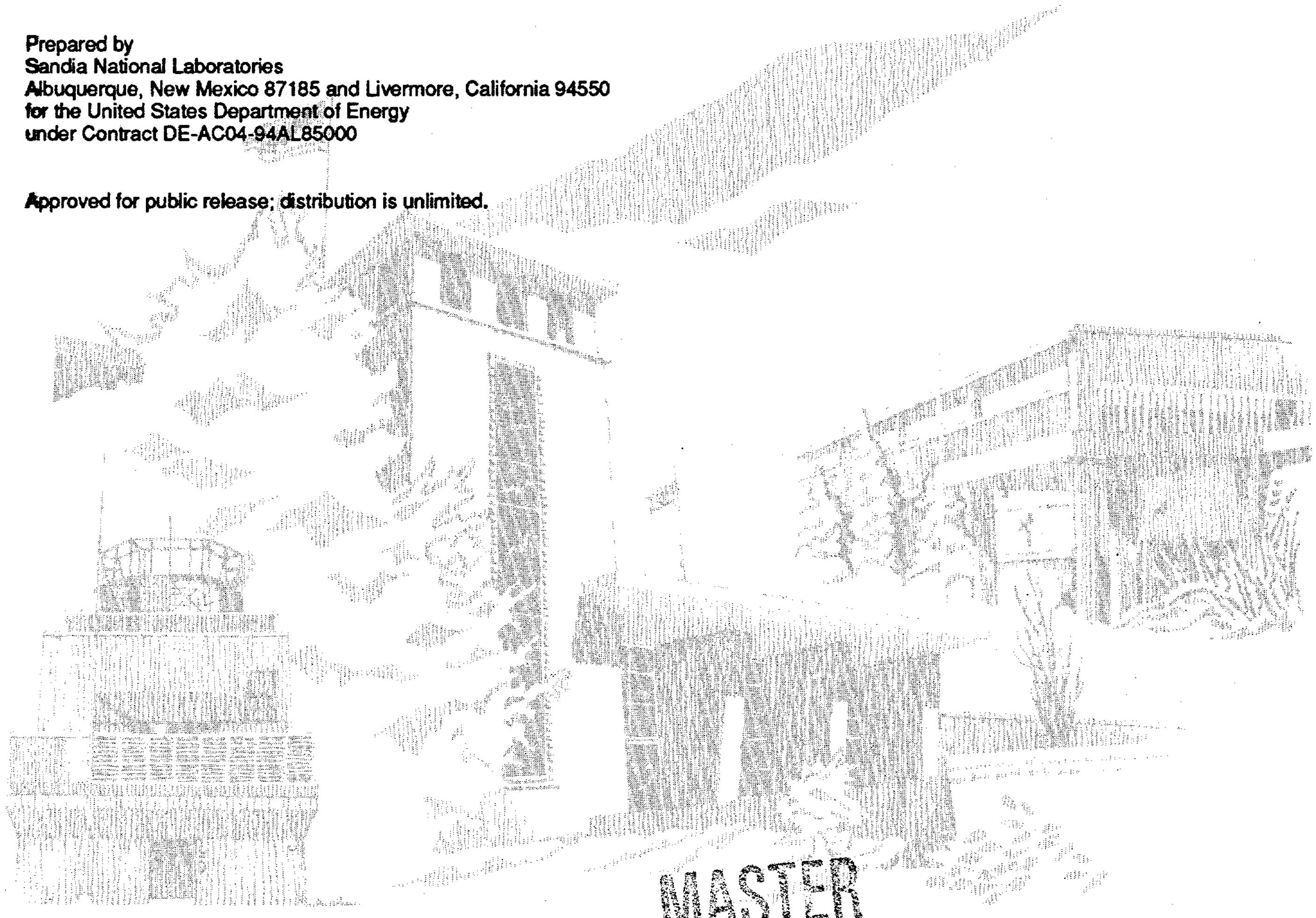

MASTER

SF2900Q(8-81)

DISTRIBUTION OF THIS DOCUMENT IS UNLIMITED 85

Issued by Sandia National Laboratories, operated for the United States Department of Energy by Sandia Corporation.

Printed in the United States of America. This report has been reproduced directly from the best available copy.

Available to DOE and DOE contractors from
Office of Scientific and Technical Information
PO Box 62
Oak Ridge, TN 37831

Prices available from (615) 576-8401, FTS 626-8401

Available to the public from
National Technical Information Service
US Department of Commerce
5285 Port Royal Rd
Springfield, VA 22161

NTIS price codes
Printed copy: A03
Microfiche copy: A01

SAND95-2342
Unlimited Release
Printed October 1995

Distribution
Category UC-703

Experimental Measurements of the Hugoniot of Stishovite

Michael D. Furnish
Experimental Impact Physics Department
Sandia National Laboratories
Albuquerque NM 87185

and

Eichi Ito
Institute for Study of the Earth's Interior
Okayama University
Japan

Abstract

We have synthesized, characterized, and performed Hugoniot measurements on monolithic polycrystalline SiO_2 samples which were predominantly stishovite (a high-pressure polymorph). Synthesis was accomplished in a multianvil press with pyrophyllite gaskets and carbon heaters. The samples had densities ranging from 3.80 to 4.07, corresponding to stishovite volume fractions of 0.7 to 0.87, a range confirmed by NMR analysis. Electron microprobe and X-ray fluorescence characterizations showed minor carbon contamination (<1%), with no other significant impurities. Samples ~1 mm thick and 3 mm diameter were tested in reverse- and forward-ballistics modes on a two-stage light gas gun, using velocity interferometry diagnostics. Impact velocities ranged from 4.0 to 6.5 km/sec. Hugoniot stresses for four tests ranged from 65 to 225 GPa. At higher stresses significant uncertainties arise due to impact tilt/nonplanarity issues. Results are consistent with earlier predictions of the stishovite Hugoniot based on quartz-centered Hugoniot data, static-compression (diamond-anvil cell) data and hydrostatic multianvil cell data. Release behavior appears to be frozen. These results are remarkable in view of the small size of the samples used. Results are compared with current EOS models.

Acknowledgments

We are happy to acknowledge the indispensable aid of the following people and institutions. First and foremost, Hideyuki Fujisawa of the Earthquake Research Institute of the University of Tokyo coordinated the sample synthesis, using a procedure developed by Eichi Ito. Clearly, without his interest and participation this project would not have occurred. Jim Asay (Sandia), Eric Rinehart, and Audrey Martinez (both FCDNA) took an interest in this project and supplied funding for the Sandia work. Ron McIntosh headed up the actual target preparation and gun/diagnostic operations at the Sandia STAR Facility, with assistance from Bill Reinhart, Carl Konrad, Clint Hall and others. Jerry Kerley supplied the input deck for PANDA for an important EOS comparison (see Appendix C). Finally, John Aidun and Lalit Chhabildas marked all over the draft version of this report, leaving me with hours of improvements ahead. Thank you all!

This work was conducted at Sandia National Laboratories under the auspices of the U. S. Department of Energy and was supported by the USDOE and the Defense Nuclear Agency under contract DE-AC04-94AL85000.

Table of Contents

Figures

Tables

This page intentionally left blank

Experimental Measurements of the Hugoniot of Stishovite

1.0 Introduction

1.1 Context

The crust and mantle of the Earth are primarily composed of silicates. The properties of these materials under compression are of interest for deducing deep-earth composition. As well, the properties of these materials under shock compression are of interest for calculating groundshock propagation. In particular, the shock compression of quartz has received considerable attention over the years.

Stishov and Popava [1961] first identified the dense phase of silica later named after Stishov as stishovite. This phase has an ambient density of 4.3 gm/cm^3, by contrast with the common quartz polymorph, whose density is 2.65 gm/cm^3, and with the intermediate-pressure polymorph coesite, whose density is about 2.9 gm/cm^3. It is stable at pressures above approximately 8 GPa and is composed of a structure in which the silicon atoms are each surrounded by six oxygen atoms in an octahedral arrangement. A pressure-temperature phase diagram of the common polymorphs of SiO_2 is shown in Figure 1.1.

A high-pressure phase of quartz observed by Wackerle [1962] in shock wave experiments was identified as stishovite by McQueen et al. [1963] on the basis of its observed transition pressure (~14 GPa) and density. McQueen et al. [1963] derived a Grüneisen ratio of $V(\delta P/\delta E)_v \equiv \gamma_0 = 0.9$, a heat of formation relative to quartz of 1.5×10^{10} erg/gm, and a bulk sound speed of 10 km/sec for stishovite. This large heat of formation indicates why stishovite is so rarely found in nature under atmospheric conditions (found primarily at geologically recent impact sites such as Meteor Crater, Arizona).

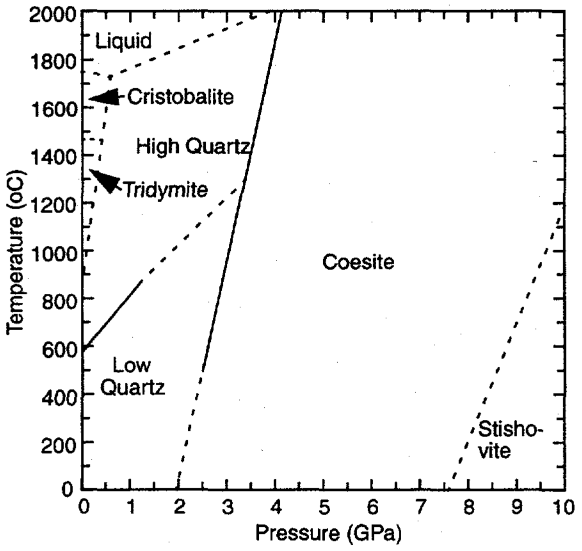

Figure 1.1. Pressure-temperature phase diagram of SiO_2 polymorphs (adapted from Hurlbut and Klein [1977]).

A number of papers were published in the early 1970s on topics related to shock compression of silica. Hugoniot experiments were performed by several Russian groups. Trunin et al. [1970] compressed quartz to ~2 TPa, concluding that no metallization discontinuities existed in that stress range (although their methods were not sensitive to metallization *per se*). Trunin et al. [1971] assessed the response of porous silica samples with starting densities of 1.15 - 2.65 gm/cm^3 to shock compression up to stresses of 40 GPa. Anan'in et al. [1974] found that the Hugoniots of monocrystalline and polycrystalline quartz differ significantly, and that initial density is also important. Theoretical modeling of the shock compression process was done by Kalanin and Pan'kov [1973] and others.

Grady et al. [1974] performed a set of experiments on shocked quartz using manganin gauges to measure stress histories, obtaining release information as well as Hugoniot states. Results from that study are shown in Figure 1.2, together with Hugoniots from other sources as noted. Interestingly, that and subsequent studies (e.g. Chhabildas and Grady [1984]) showed that releases are "frozen" down to about 8 GPa, then a transition to a lower-density phase occurs. Grady et al. [1974] inferred that any ongoing shock transformation behind the shock front is very slow, a conclusion also reached by Podurets et al. [1976] based on the observation that Hugoniot states in the mixed phase zone did not appear to depend on peak stress duration.

In this same time period various data were gathered on the microscopic nature of shocked quartz, producing the following conclusions:

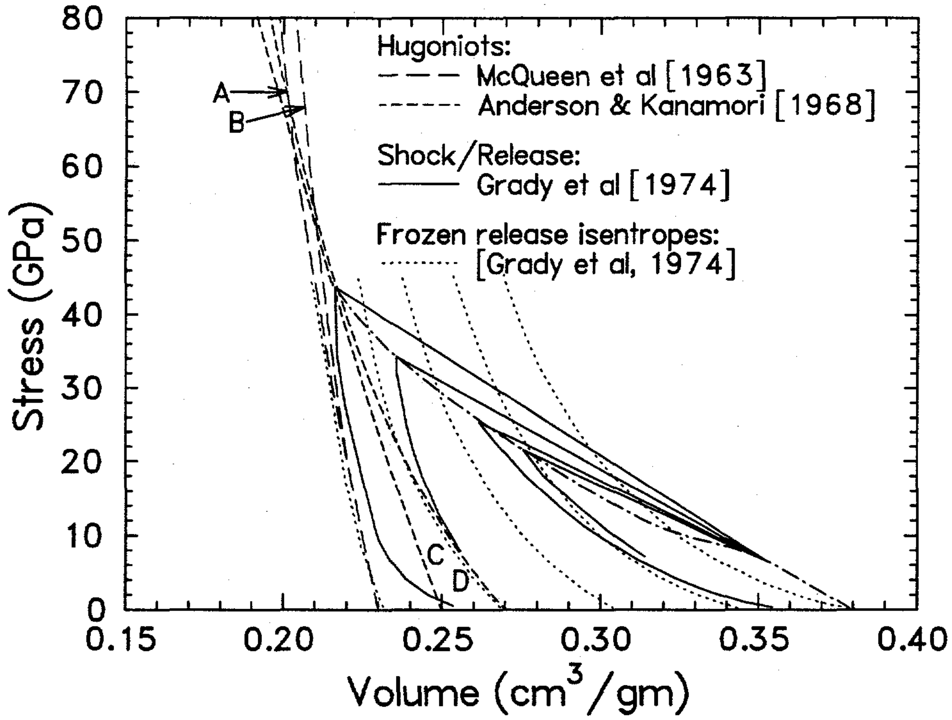

Figure 1.2. Quartz Hugoniots and release paths (experimental and theoretical). Curve "A" is centered at $\rho_0 = 4.3$ gm/cm^3; "B" at 2.65 gm/cm^3 [McQueen et al, 1963]; "C" at 4.0 gm/cm^3; and "D" at 3.7 gm/cm^3 [Anderson and Kanamori,

- Irreversible vitrification occurs on shocking of quartz to stresses above about 6 GPa [Anan'in et al, 1974].
- Yielding at the Hugoniot elastic limit corresponds to fragmentation of monocrystals, melted boundaries and high temperature gradients. Increasing stress gives increasing sizes of melt zones [Anan'in et al, 1974].
- Coesite is formed in a geological process by shocking to stresses of 30 - 55 GPa. This is higher than the stress range required to form stishovite (12 - 45 GPa [Stöffler, 1971] or 9 GPa up [Kleeman and Ahrens, 1973]), suggesting that coesite is formed "on the way down." Both minerals are highly sensitive to subsequent annealing processes [Stöffler, 1971]. Both of these minerals tend to be small fractions of the recovered rock mass (0.005 - 4% for stishovite; 7- 40% for coesite). The stress levels required to produce some degree of transformation in shock experiments agree with the conditions required in static compression experiments.
- The shock process may produce a short-range ordered phase corresponding to the stishovite structure, which reverts to a glass upon release [Kleeman and Ahrens, 1973].

An intriguing possibility was raised by an experiment by Pavlovskii [1978]. A magnetic-pinch experiment appeared to cause the collapse of a silica sample to a density of 10 gm/cm^3 at a stress of 125 GPa and a temperature of roughly 1000K. This experiment has been criticized as vulnerable to misinterpretation; for example, a necking of the sample could give misleading results. Nevertheless, the result is sufficiently interesting to bear confirmation. Single-shock loading of quartz, however, cannot produce these conditions. At a stress of 125 GPa, temperatures of nearly 5000K are expected. Fritz and McQueen [1984] performed double-shock experiments to produce stresses of 145 GPa, although no evidence for a catastrophic density collapse was observed.

Subsequent work has proceeded along several lines. Waveform measurements on X-cut quartz using a "reverberation" configuration allowed Chhabildas and Miller [1985] to confirm the "frozen" releases noted above. Their wave speed measurements suggested a further transition (possibly melting) occurring for stresses above 80 GPa. Quasi-static compression in a diamond anvil cell produced an amorphous phase at a temperature of 300K and pressure of 25- 35 GPa [Hemley et al, 1988], suggesting a sluggish breakdown of the SiO_4 tetrahedra under these conditions. Compression of stishovite apparently causes a structural distortion to the $CaCl_2$-type structure above 80 GPa (Yagi et al. [1990], concluded from x-ray diffraction spectra using a laser-heated diamond anvil cell). Computational (molecular dynamics) simulations of the microstructure by Tsuneyuki et al. [1989] gave the same deformation to the $CaCl_2$-type structure, and, for stresses to 250 GPa, gave no transition to the $Pa\overline{3}$ phase, which is predicted to be denser.

1.2 Objectives

Prior to the present study, no shock compression studies using stishovite samples had been performed. The goal of the present study is to measure the Hugoniot of silica beginning with stishovite samples (initial densities of 3.8 - 4.2 gm/cm^3).

Such measurements provide a check on the existing theories of the stishovite equation of state in two ways. First, the thermal regimes exercised are quite different than for the Hugoniot centered on quartz, as shown in Table 1.1. Quantitative deviations from the Hugoniot centered on quartz are expected (Figure 1.2), and qualitative deviations are possible if new phases become accessible in this lower-temperature regime.

Table 1.1. Comparison of specific energies for Hugoniots centered on quartz and stishovite

Stress		E (MJ/kg)*	
(GPa)	$\rho_0 = 4.29$ gm/cm^3	$\rho_0 = 3.70$ gm/cm^3	$\rho_0 = 2.65$ gm/cm^3
40	0.37	1.17	3.27
60	0.79	2.00	5.07
80	1.25	2.86	6.94

*Using Hugoniot curve "B" of Fig. 1.2 for $\rho_0 = 2.65$ gm/cm^3; curve "A" otherwise

Second, the starting material is known to be stishovite (with some impurities and some back-transformed quartz and coesite), so at high stress levels it is likely to remain stishovite. In shock experiments using quartz or fused silica samples, the identity of the high-pressure phase is presumed to be a combination of a short-range-ordered glass, a melt and a cryptocrystalline state, all with an average silicon coordination value of approximately six. This distinction is not likely to result in qualitatively different behavior, but the possibility must be borne in mind.

Sample preparation and characterization are discussed in Section 2. This aspect of the present study is critical to interpretation of the final results.

Sections 3 and 4 discuss the two methods employed for shock wave studies of stishovite in the present study. The samples employed were very small, so were near the limits of the resolution of present characterization methods using gun launchers. Therefore it seemed prudent to use two complimentary experimental methods, with different sets of uncertainties, to arrive at a final result whose credibility could be evaluated.

The first shock-wave method, referred to as "reverse-ballistics," uses a configuration with the sample in the projectile. A velocity interferometer is used to measure a waveform in the target. The peak (plateau) level of this waveform is the quantity of interest. The sample density, projectile velocity and plateau level determine the Hugoniot.

The second method, referred to as "forward-ballistics" or "transmitted wave," uses a configuration with the sample in the target. A velocity interferometer is used as before. For this case, the time-of-arrival of the wave at the back side of the sample (hence the shock speed in the sample) is the quantity of interest. Combined with the projectile velocity, a knowledge of the shock properties of the projectile, and the sample density, it determines the Hugoniot.

2.0 Sample Preparation and Characterization

2.1 Synthesis

Samples of monolithic, polycrystalline stishovite (actually, a mixture of SiO_2 polymorphs) were prepared in the laboratory of Hideyuki Fujisawa of the University of Tokyo. A multianvil press, with tungsten carbide anvils, pyrophyllite gasket and graphite heaters, was used. The starting material was an activated silica (a gel). The sample was held at 1100 °C and 10 GPa for slightly over an hour, with a slow cool-down. Two samples were prepared this way; one was recovered whole, while the other was recovered in six disks (apparently fractured during the cooling/depressurization phase). The samples were about 3 mm diameter and 8 mm long. From this, samples about 1 mm thick and 3 mm diameter were obtained. The original samples are shown schematically in Figure 2.1.

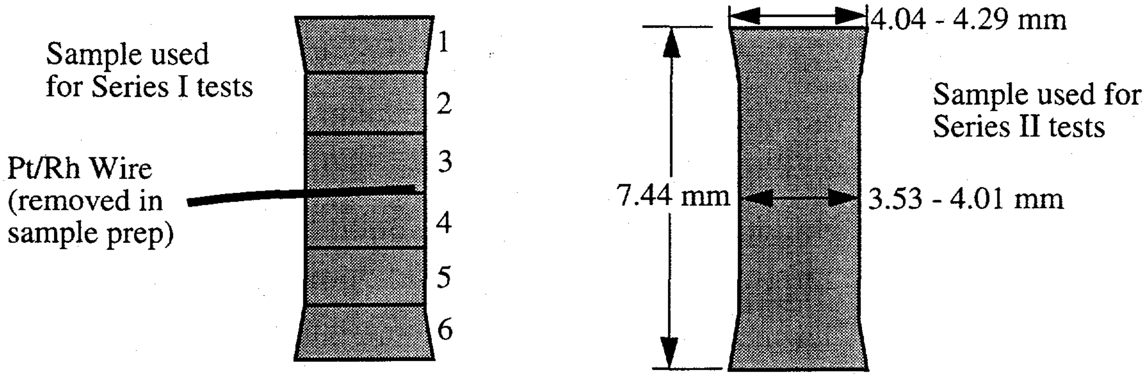

Figure 2.1. Samples obtained from multianvil press, shown in as-received condition. Sample numbers (left hand sample) are consistent with labels later in this document.

2.2 Characterization

Eight types of sample characterization were performed on the samples used for the Series I tests. Two of these (visual characterization and density measurements) were repeated for the samples used for the Series II tests. Selection criteria for choosing samples to be used in impact tests are discussed at the end of this section.

Visual characterization

All of the samples used had dark, fairly uniform appearances, and were reminiscent in size, shape and texture of Halazone® tablets used by backpackers for water purification. Some light-colored crystals were seen (to ~60 µm); dark-colored groundmass appeared to be much finer. Minor corner chipping was found on some samples after surface grinding to prepare for impact testing. Photographs of all samples used are shown in Figure 2.2.

Comments and approximate dimensions for the individual samples are shown in Table

Comments and approximate dimensions for the individual samples are shown in Table 2.1. It is interesting that the original sample from which Samples 1 - 6 was derived fractured into relatively equally-sized disks. This equal spacing of fractures suggests a link to cooling/depressurization stresses, although the actual cause of these fractures is uncertain.

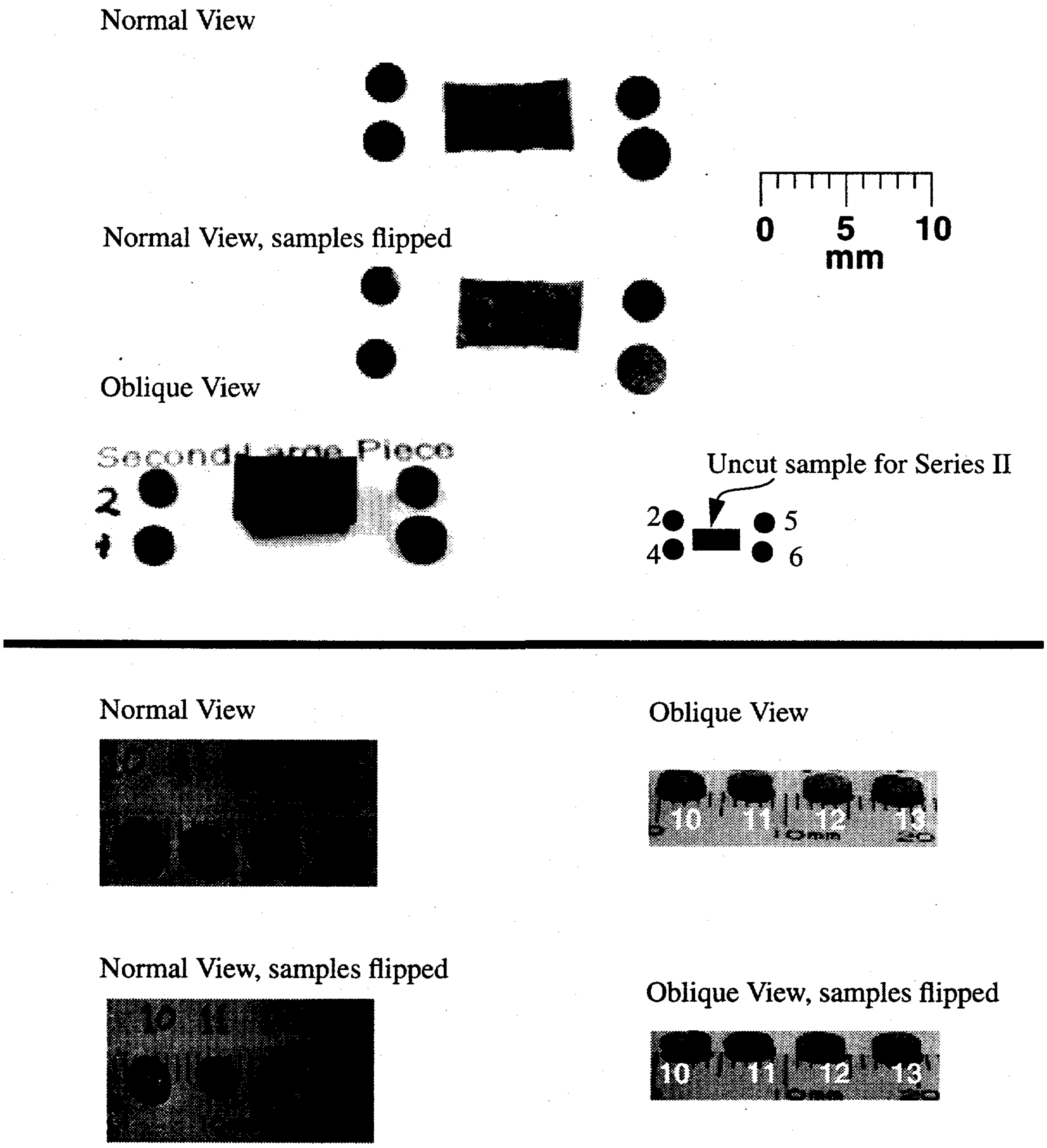
Normal View

Normal View, samples flipped

Oblique View

Uncut sample for Series II

Normal View

Oblique View

Normal View, samples flipped

Oblique View, samples flipped

Figure 2.2. (Top) Photographs of stishovite samples used in Series I and uncut sample later used for Series II tests. (Bottom) Photographs of stishovite samples used in Series II (prepared for impact testing). Insets show sample arrangements in photos.

Density measurements

Density measurements were performed, both by immersion and by geometric measurements combined with weighing. The sensitivity of the immersion measurements to small entrained bubbles (which were difficult to avoid reliably) led us to discard those results in favor of the geometric method. Diameters and defect dimensions were determined using a binocular microscope equipped with a ruled eyepiece, calibrated according to a machin-

Table 2.1. Sample descriptions

	Diameter		Thickness		
Sample #	Max. (mm)	Min. (mm)	Max. (mm)	Min. (mm)	Comments
			Series I (Reverse Ballistic) *(Samples as-received)*		
1	3.07 3.49	2.90 3.21	1.55	1.37	(Different sized faces) Weak foliation along large dia Dark and very light gray xtals 25-40 µm on large face.
2	2.95	2.64	1.75	1.27	Texture dominated by dark crystal masses ~150 µm apart individual grains 5 - 13 µm
3	2.77	2.49	1.27	1.02	Texture like #2 50 µm piece of Pt/Rh wire
4	2.79	2.62	2.03	1.80	Similar texture to #2, 3.
5	2.97	2.67	1.45	1.45	Few 50-75 µm light crystals dark, much finer groundmass
6	3.05 3.49	2.77 3.28	2.16	1.98	Small face similar to 2 - 5; large similar to large face of 1
			Series II (Forward Ballistic) *(Samples after machining)*		
10	4.05 3.90	3.90 3.80	0.846		Dark side Light side (Hole ~0.4 x 1 mm x 0.1 mm deep near middle of dark side prior to final lapping)
11	3.75 3.70	3.5 3.45	0.930		Large face good; small has gouge 1.1 x 0.5 wide x 0.01 -0.12 mm deep near edge
12	3.82 3.78	3.70 3.65	0.980		Both surfaces very clean
13	4.10 3.89	3.90 3.60	0.977		Chipped edge (0.7 x 0.2 x 0.05 mm chip volume)

ist's ruler. Thicknesses were measured by means of micrometer-equipped calipers. All geometric and mass measurements were made after each sample's surfaces were ground flat and parallel in preparation for impact testing.

Density results are shown in Table 2.2. For each of these samples, an estimate is made of the stishovite fraction, based on Equations 2.1. Inclusion of significant amounts of coesite ($\rho_0 = 3.01$ gm/cm^3) would tend to depress the stishovite fraction somewhat (~1 - 8% for replacement of quartz by coesite in amounts 10 - 100%).

$$\rho_{0(\mathrm{stish})} \equiv \rho_S = 4.29 \text{ gm/cm}^3 \text{ (Density of stishovite)}$$

$$\rho_{0(\mathrm{quartz})} \equiv \rho_Q = 2.65 \text{ gm/cm}^3 \text{ (Density of quartz)}$$

$$\phi_{SV} = (\rho - \rho_Q)/(\rho_S - \rho_Q) \text{ (Volume fraction comprised of stishovite)} \qquad \text{(Eq's. 2.1)}$$

$$\phi_{SM} = \frac{\phi_{SV}\rho_S}{\phi_{SV}\rho_S + (1 - \phi_{SV})\rho_Q} \text{ (Mass fraction comprised of stishovite)}$$

Table 2.2. Density measurements for stishovite samples

Shot #	Geometric Density (ρ_G) (gm/cm^3)	Sample #	Stishovite Fraction (from ρ_G) (Vol.; ϕ_{SV})	(Mass; ϕ_{SM})	Immersion Density (ρ_I) (gm/cm^3)
Series I (Reverse Ballistic)					
1	3.985	2	0.814	0.876	3.61
2	4.067	4	0.864	0.911	3.83
3	4.070	5	0.866	0.913	3.54
4	3.800	6	0.701	0.791	3.96
--		1			3.58
--		3			4.76
Series II (Forward Ballistic)					
10	3.822	10	0.715	0.802	3.90*
11	3.959	11	0.798	0.865	3.90*
12	3.954	12	0.795	0.863	3.90*
13	3.833	13	0.721	0.807	3.90*

*Immersion densities for Series II were of one sample, later divided into Samples 10 - 13.

Nuclear Magnetic Resonance

NMR (^{24}Si) characterization of the unbroken piece of stishovite eventually used for the Series II tests was performed by Spectral Data Services (Champaign, IL). with 5 second and 30 second relaxation times. The resulting plot is shown as Figure 2.3. The region between Channels 1200 and 1400 corresponds to four-coordinated silicon (coesite and quartz); that between channels 1600 and 1800 corresponds to six-coordinated silicon

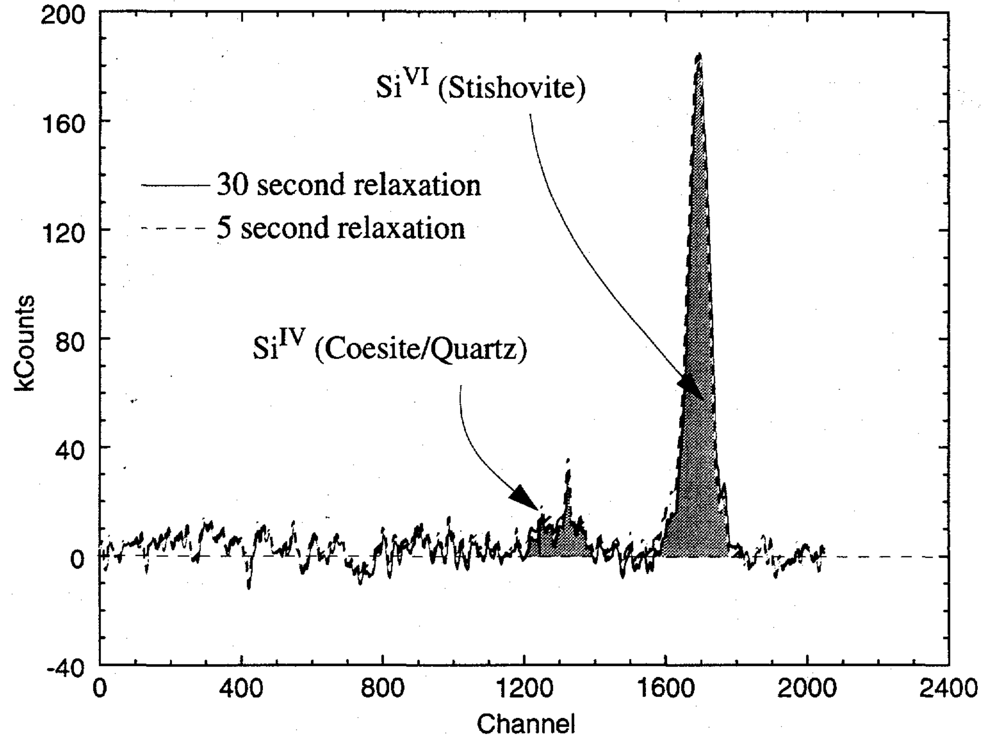

Figure 2.3. NMR analysis of stishovite sample cut to give samples for Series II tests.

(stishovite). The conclusion is that more than 85% of this sample (by mass) is stishovite. Due to the nature of the sample (cylindrical and somewhat fragile), magic-angle spinning was not used. Since the expected peaks are quite clear in the spectra, this did not seem to compromise the conclusions.

Electron microprobe analysis

Electron microprobe results showed that there was minor carbon contamination (less than 1%) and no other contamination. The analysis measured contamination by C, Fe, Mg, Ni, Cu and W, as well as Si presence. In addition, the wire on Sample # 3 (sample not used in shock tests) was found to be Pt-Rh, as might be expected for an embedded thermocouple. Minor surficial iron/chromium particulate contamination was found on some rough surfaces; we presume this was removed during the grinding process later.

X-ray fluorescence analysis

Both wavelength-dispersive and energy-dispersive X-ray spectroscopy were used to measure molar ratios of elements for the Series I stishovite samples (prior to final grinding). Several different operating conditions were used for all analyses. Silicon was the primary element detected, as expected. Aluminum was a trace component in Samples #1 and 4 (Sample 4 was used in test St-2; Sample 1 was not used in shock tests), while trace amounts of iron were present in Samples #4 and 6. No indication of Mg, Ni, Cu or W contamination was found. This method is not sensitive to carbon, some of which may be present from the graphite heaters.

X-ray transmission images

X-ray transmission images were made for samples 1 - 6, using 40 kV X-rays. Both face-on and side views were recorded. None of the face-on views showed detail other than the outline of the samples. The side view of Sample 1 showed a significant contrast change about 20% of the distance from the edge to the center on one side (the other side was obscured by the mounting). Sample 2 showed a slightly lower stopping power within ~5% of the thickness of one face, although that thickness was roughly that expected to be lost to grinding. We concluded that, with the possible exception of Sample 1, no structural variations were found which might compromise the results.

Ultrasonic measurements of sound velocities

Ultrasonic measurements of longitudinal and shear sound velocities were conducted by comparing direct transducer-transducer coupling with coupling through the samples. 50 MHz transducers were used for longitudinal measurements and 20 MHz were used for shear measurements. Results are shown in Table 2.3. Samples 1, 4 and 6 showed some low-frequency wave generation, suggesting microcracks or possible porosity. Significant porosity is unlikely in view of the synthesis procedure for these samples; microcracks due to cooling and decompressing, however, are not surprising.

Table 2.3 Sound velocity measurements for Series I stishovite samples

Shot #	Sample #	Sound Vel. (km/sec) Longitudinal	Shear
1	2	8.90 ± 0.04	5.77 ± 0.03
2	4	9.12	5.65
3	5	9.74	5.84
4	6	7.09	4.65
--	1	6.77	4.55
--	3	9.03	5.42

Ultrasonic microscopy and profiles

Ultrasonic profiles and ultrasonic microscopy (at surface and depth of 15 μm) showed contrasts on scales to 30- 40 μm, which may also correspond to an upper limit on grain size. Occasional features with the appearance of 20 - 30 μm wide canyons were observed, possibly corresponding to zones of low longitudinal wave speed due to mechanical decoupling between grains.

Selection criteria

The issue is the choice of samples to use for tests. The primary differences between samples lie in the size of the samples, initial densities, and surface features which might interfere with a successful experiment. Smaller samples, samples with a lower density (lower stishovite content), and samples with imperfect surfaces are either eliminated from testing or used on the tests with the highest probability of failure (generally, first in a series).

In Series I, two samples could be excluded to meet a goal of 4 tests. Sample 3 was the thinnest of those available for Series I, was the most at risk for contamination by the thermocouple wire, and showed an anomalous density in the initial measurements; it was therefore excluded. Sample 1 and Sample 6 were both suspect on the basis of their positions on the ends of the original sample; since Sample 1 had the lower density and was thinner, it was excluded. Although a parallel argument regarding density could have been made for excluding Sample 5, we did not have the luxury of excluding three samples in Series I.

For Series II, no samples could be excluded because only four were available. Sample 10 had a significant divot near the center of one face, and on thinning to 0.846 mm to remove most of this divot became the thinnest sample. It was therefore used on the first test in this series.

3.0 Impact Experiment Designs

3.1 Reverse-ballistic (Series I)

A specialized reverse-ballistic geometry as shown in Figure 3.1 was employed to measure Hugoniot and release properties. This configuration uses one VISAR (Velocity Interferometry System for Any Reflector [Barker and Hollenbach, 1972]) for monitoring the

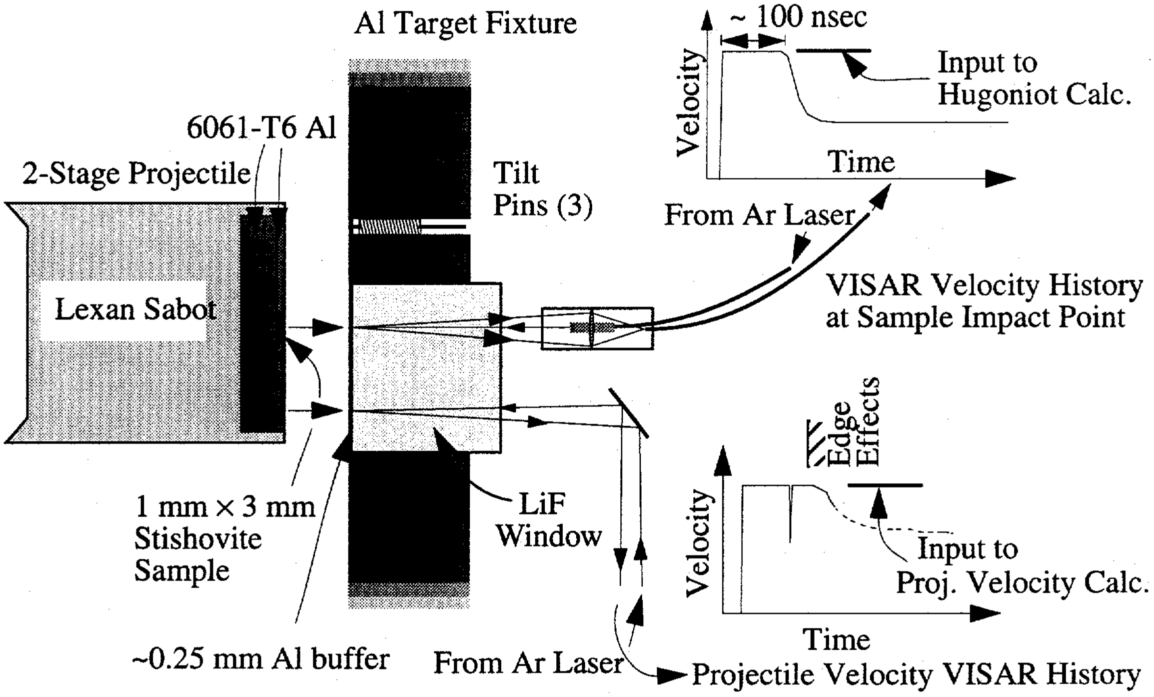

Figure 3.1. Configuration for reverse-ballistic (Series I) stishovite tests.

waveform in the portion of the target most strongly affected by the stishovite sample. It uses a second VISAR to measure the projectile velocity (see below). These will be referred to as the "Sample" and "Projectile Velocity" VISARs.

The waveform obtained from the sample VISAR is used for computing the sample Hugoniot and release properties. The details of this method are presented elsewhere [Furnish, 1993a,b]. In brief, the Hugoniot is calculated from the sample density, projectile velocity and plateau level (shown as "input to Hugoniot calculation" in Figure 3.1). The procedure for calculating release paths is to model the tests with the Lagrangian wavecode WONDY V [Kipp and Lawrence, 1982], using a Mie-Grüneisen loading behavior and an unloading behavior governed by a modulus expressed in Equation 3.1. The coefficients B_i are varied until the experimental waveform is reproduced, at which point the stress/density behavior may be calculated from Eq. 3.1.

$$\frac{\delta P}{\delta V} = \frac{-B_0}{V}\left(1 + B_1\chi + B_2\chi^2 + B_3\chi^3\right)\text{, where } \chi \equiv \frac{P}{P_{Hug}} - 1 \qquad \text{(Eq. 3.1)}$$

Precise alignment requirements for this VISAR led us to choose a fiber-optic configuration.

Projectile velocity for tests on this two-stage gun system would ordinarily be measured by a MAVIS (Magnetic Velocity Induction System) or by flash X-rays. Either method, however, requires approximately 13 inches of projectile free-flight, which poses an unacceptable risk of allowing the sample to "miss" the portion of the target monitored by the VISAR monitoring the impact point of the sample. The sample diameter is only ~3 mm. Hence, a second VISAR was used to measure the projectile velocity. The laser for this system was directed to a point 9.525 mm from the point monitored by the sample VISAR.

Note that both velocity interferometers must yield unambiguous records for a test to be considered successful. Without meaningful data from the projectile velocity VISAR, the projectile velocity is only known to 3 - 5%. Without meaningful data from the sample VISAR, no sample-specific information is available and a Hugoniot cannot be derived. Since both VISARs are sampling locations near the edges of critical components in the projectile (the sample for the Sample VISAR and the impactor plate for the Projectile Velocity VISAR), edge effects are expected to begin affecting the velocity profiles a very short time after impact (100 - 200 nsec). Consequently, the entire experimental design is not as robust against failure as we would have desired. However, we are able to tell whether a given experiment was successful by the shapes of the observed waveforms.

Some of the geometric constraints of this geometry are depicted in Figure 3.2. For example, the offset LiF window precludes the use of a fourth rear-surface tilt pin for impact planarity determination (the three remaining pins provided sufficient information). The most difficult aspect of this design was in arranging for the spots monitored by the two velocity interferometers to be sufficiently close together that the edge effects of the projectile did not immediately contaminate the projectile velocity VISAR waveform.

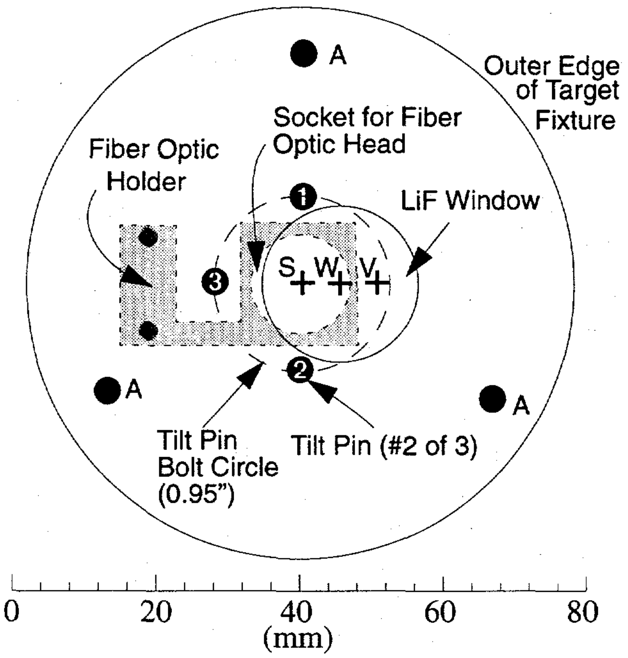

Key:

A	Mounting hole
S	Sample Impact Point
W	Window Center
V	Projectile Vel. VISAR point

Note that the tilt pins are positioned on a circle which lies just inside the impact circle of the projectile.

Figure 3.2. Plan view of Stishovite Series I targets.

3.2 Transmitted-wave (Series II)

A second configuration was chosen to compliment the Series I experiments. This configuration utilized a transmitted wave (forward ballistic) arrangement, as shown in Figure 4.1. Several differences between this configuration and the reverse ballistic configuration discussed in Section 3 should be mentioned:

- The critical measurement is the arrival time of the shock at the interface monitored by VISAR, rather than the plateau velocity in the wave profile.
- Precise projectile position is less critical than for the reverse-ballistic configuration. Hence projectile velocity could be measured by means of a MAVIS.

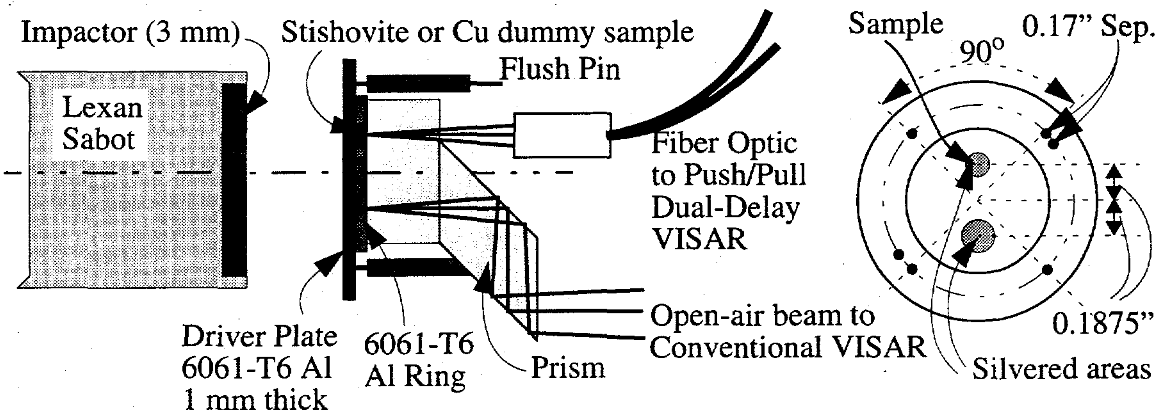

Figure 3.3. Configuration for forward-ballistic (Series II) stishovite tests

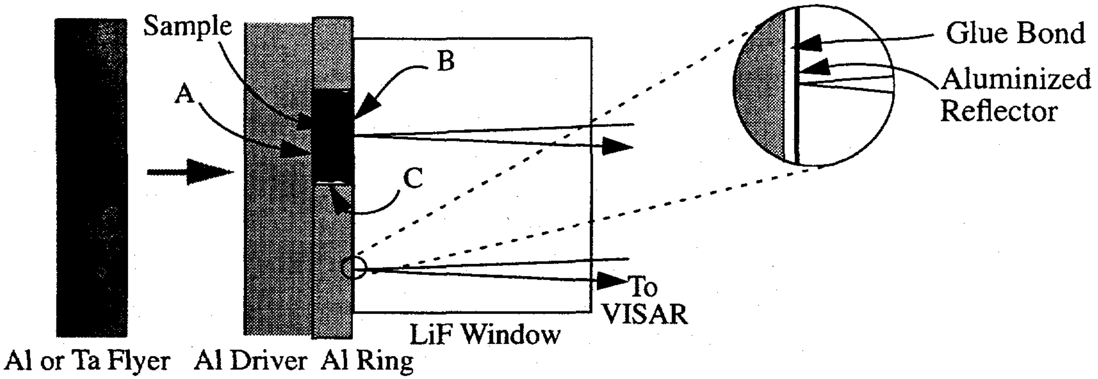

Figure 3.4. Important interfaces for forward ballistic configuration. (A) Sample-driver interface; gap delays shock; (B) Sample-window interface; gap delays shock; (C) Lateral interface; gap slightly accents edge effects.

- Precise timing of the impact must be measured here in order to deduce shock transit time, and hence shock velocity.
- Higher stress levels may be achieved by using high-impedance impactors (e.g. tantalum), while still maintaining a relatively simple set of wave interactions.

Measuring arrival time with adequate accuracy is the most difficult aspect of experiments using this configuration. The expected shock transit time for these samples is ~90 nsec, so timing accuracies to ~2 nsec are required to achieve 2% error levels. Previous experience has demonstrated that the flush pins alone provide slightly poorer timing accuracy. Hence a second VISAR (referred to as the timing VISAR) was added to provide a timing reference. Details of the timing procedure are presented in Appendix B.

For these tests to be successful, it was necessary to pot the machined samples into a precut hole in an aluminum disk ~1 mm thick (referred to as an aluminum ring in Appendix B), then lap this plate (hand lapping) until the sample face was flush with the plate surface on both sides. In this way it could be assured that the shock entered the sample at the same time as it entered the surrounding material, and that any glue bond thickness between the sample and the window was minor. Details are shown in Figure 4.2. The surface monitored by both VISARS was the silvered surface of the LiF window (glued to the sample and the disk surrounding it).

Determination of the sample shock transit times (hence shock velocity) proceeded as follows. For more detail, please consult Appendix B. Interferometer fringe traces from the two VISAR systems were recorded on electronic digitizers, together with timing fiducials. The fiducials were used to correlate digitizer traces. Each set of fringes was recorded on two sets of digitizers, allowing some ability to assess reading errors. In addition, selected fringe records from the two VISAR systems (the Data 1 traces) were recorded on a system with two lockstep channels, allowing a fiducial-independent check on relative timing of the two traces. All data and fiducial transmission times were carefully measured, including wire, light beam, fiber optic, intra-VISAR travel times and photomultiplier response times.

Tilt of the impact (affecting the relative times at which the shock entered the target opposite the points monitored by the two VISAR systems) was assessed by the standard set of 4 rear-surface tilt pins (coaxial, self-shorting), complemented by 2 additional pins. The first of these pins to short was also used to trigger the digitizers and generate the timing fiducial. Plots of the outputs of these pins were used to determine consistency of the pin firing times.

The following steps were used to deduce the sample shock transit time after the test (see Appendix B for details):

1. Calculate the time of shock arrival for the Sample VISAR relative to that for the Timing VISAR, using fiducials and accounting for relative signal travel times, and assessing consistency amongst the records available from the test.
2. Calculate the shock transit time through the aluminum (at the Timing VISAR point); add this to the difference between the shock arrival times at the sample and that at the timing VISAR location.
3. Correct for impact tilt as determined from the tilt pins, assessing tilt pin records for clearly erroneous firing times.

From this procedure the Hugoniot states were derived. The Rankine-Hugoniot steady-wave relations were used, although the present results are not sensitive to the steady-wave assumption.

4.0 Results

4.1 Hugoniot states

Four tests yielded usable stishovite material properties data, including one reverse-ballistic test and three transmitted-wave tests. All provided Hugoniot data. Only the reverse-ballistic test provided release data. Critical experimental parameters of these four tests are shown in Table 4.1. For more details, please consult Appendices A and B.

Table 4.1. Test matrix

Test	ST2*	ST11	ST12	ST13
Projectile. Vel. (km/s)	4.01	4.88	4.98	6.54
Impactor Material	--	Al	Ta	Ta
Impactor Thickness (mm)	--	2.995	1.030	0.779
Sample measurements -				
Thickness (mm)	0.859	0.931	0.978	0.977
Diameter (mm)	2.40	3.600	3.700	3.872
Density (Mg/m^3)	4.067	3.959	3.954	3.833

*Reverse-ballistic test; sample backed by 160 μm epoxy.

Table 4.2. Stishovite Hugoniot states from present experiments.[1]

Shot #	Proj. Velocity km/sec	Strain	ρ_0 gm/cm^3	Particle Vel km/sec	Pressure GPa	ρ gm/cm^3	Shock Vel. km/sec	ρ/ρ_0	Specific Vol cm^3/gm
ST2	4.01	0.16(4)	4.07(30)	1.50(12)	59(4)	4.8(5)	9.6(1.4)	1.19(5)	0.207(19)
ST11	4.88	0.24(3)	3.96(10)	2.06(9)	69(3)	5.2(3)	8.5(7)	1.32(6)	0.191(9)
ST12	4.96	0.34(4)	3.95(10)	3.44(8)	136(9)	6.0(4)	10.0(9)	1.52(10)	0.166(11)
ST13	6.54	0.33(10)	3.83(8)	4.36(25)	223(36)	5.8(1.1)	13.4(2.7)	1.48(28)	0.176(28)

---

[1] Numbers in parentheses represent uncertainties in the last 1-2 digits of the quantity.

Values of the Hugoniot quantities are shown in Table 4.2. Experimental uncertainties are propagated in quadrature to give the quoted uncertainties in the values of the Hugoniot quantities. For the reverse-ballistic experiment ST2, the important uncertainties are projectile velocity, plateau ("observed") velocity and initial density. For the transmitted-wave experiments, the most important uncertainty was the impact planarity, with sample density and impact velocity also representing significant uncertainties.

These results are plotted in Figure 4.1 (detail of stress/density representation in Figure 4.2), together with the following additions:

1. Hugoniot data for quartz and various quartz-rich rock materials (various sources).
2. A theoretical curve [Boettger, 1992] which fits the above quartz-centered Hugoniot data well.
3. A tabular Sesame equation of state generated by PANDA [Kerley, 1988], based on a cold curve represented by a Birch-Murnighan expression with ρ_0 = 4.3 gm/cm3, B_0 = 3.8 GPa and B_0' = 3.8 [G. I. Kerley. personal communication]. Results are plotted for three initial densities. See Appendix C for details
4. A compression curve extrapolated from the 0 - 11 GPa hydrostatic compression (multianvil) data of Sato [1977].
5. Diamond-anvil compression data of Tsuchida and Yagi [1989], where specific volume is calculated from X-ray diffraction data assuming a transition to the $CsCl_2$ structure at approximately 90 GPa. These data may slightly underestimate compressibility due to the axial X-ray diffraction used, although the error should be small.
6. A release path derived from test ST2 (see Section 4.2).

Since the samples have initial densities ranging from 3.83 to 4.07 gm/cm^3, it is useful to compare the present Hugoniot results with the PANDA EOS calculations assuming a starting density of 3.9 gm/cm^3. The agreement is within the uncertainty bars for all tests except ST12.

There is no suggestion of a major collapse as claimed by Pavlovskii [1978]. The Pavlovskii density increase would have been to a density of 10 - 11 gm/cm3 at a stress of 120 - 150 GPa, based on Pavlovskii's measurements.

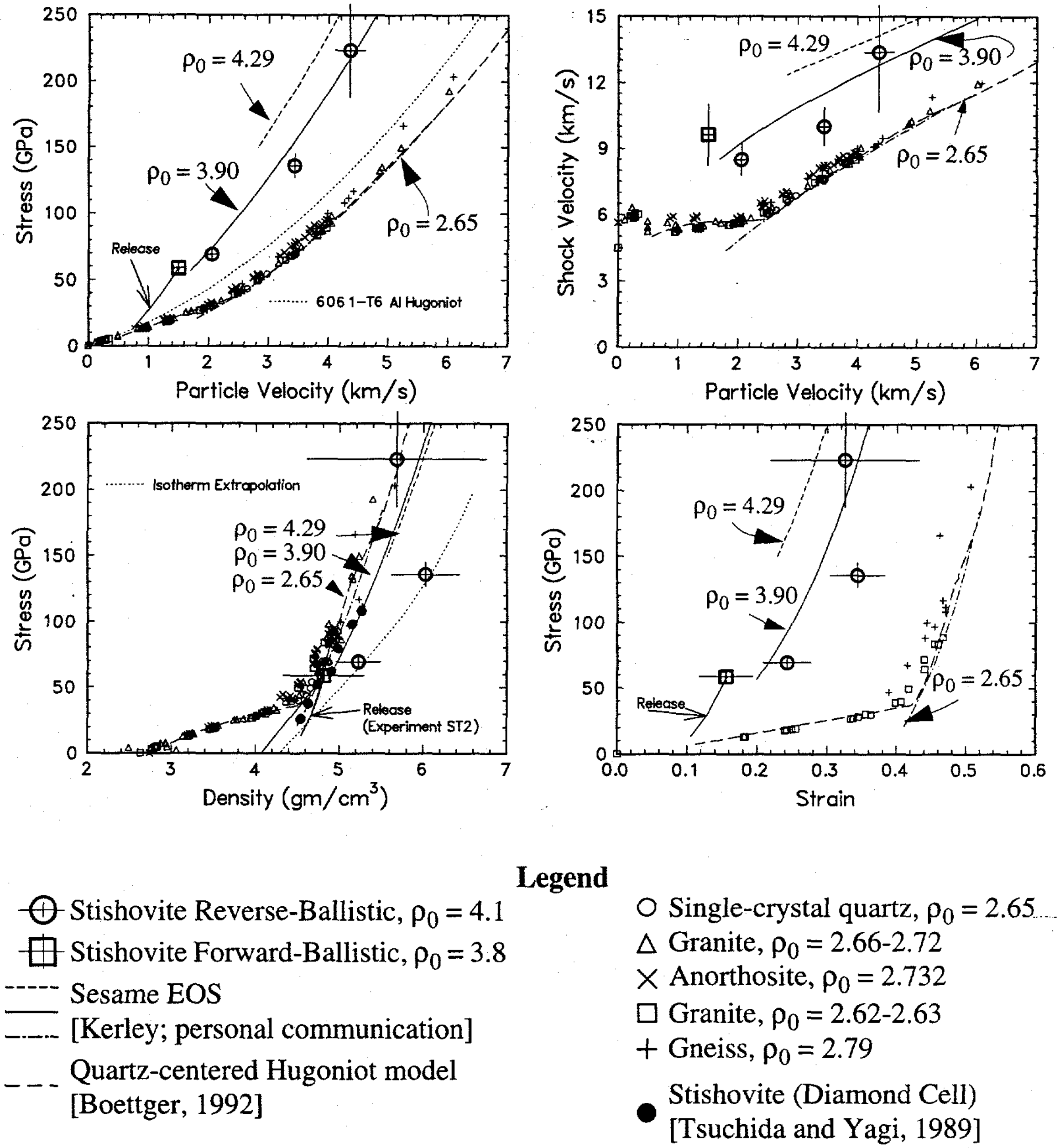

Figure 4.1. Hugoniot of stishovite (present series), compared with representative quartz-centered data and calculations. Stress/density plot is enlarged in Figure 4.2.

Although there is some spread in the Hugoniot data for the rock materials shown in Figure 4.1, it is narrow enough that conclusions drawn from a study of quartz shock properties would appear to be relevant to this entire family of materials.

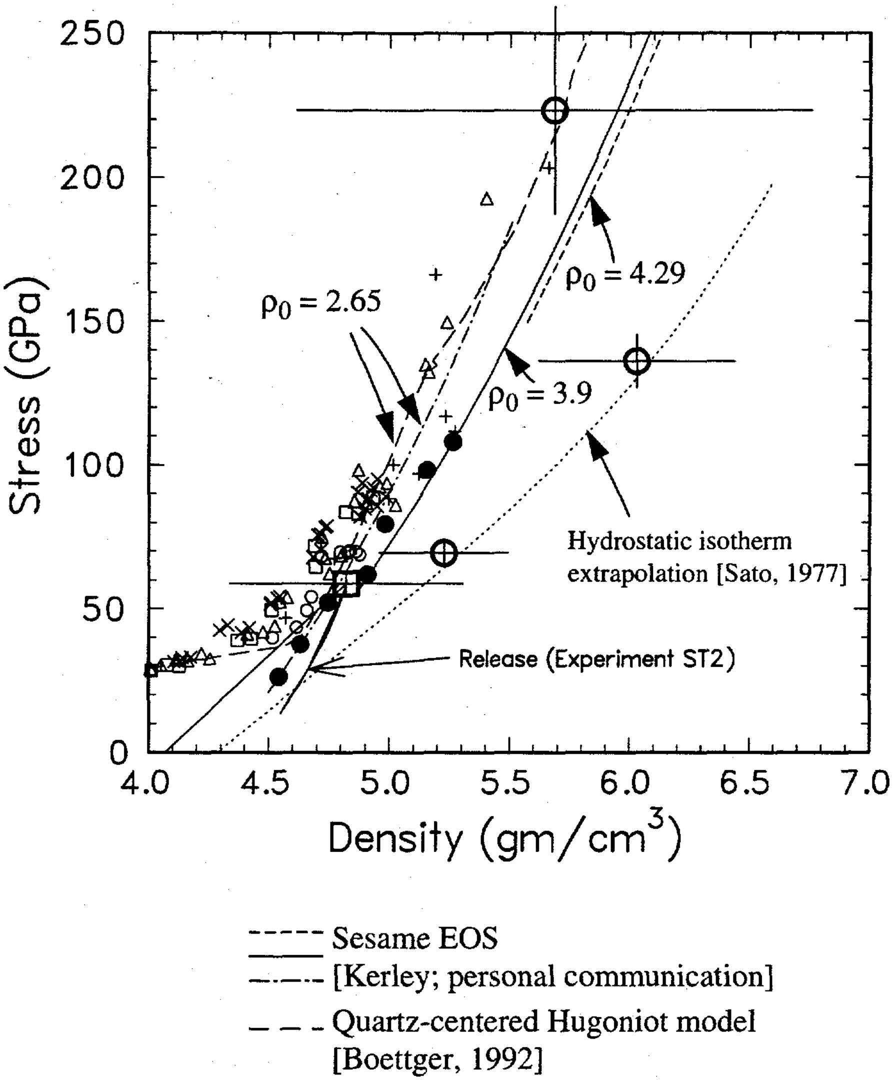

Figure 4.2. Detail of stress-density relations for Hugoniot of stishovite (present series), compared with representative quartz-centered data and calculations (complete legend in Fig. 4.1).

4.2 Release properties and waveform modeling

The waveform from the reverse-ballistic experiment ST2 was modeled using a variable release description to extract a release path. The procedure is discussed in Section 3.1. The resulting release path is shown in Figures 4.1 and 4.2 (above). For comparison with the earlier predictions of stishovite behavior, this release and the Hugoniot values are plotted against the curves of Figure 1.2 in Figure 4.3. The present release is found to agree very closely with the "frozen" release description inferred by earlier workers (e.g. Grady et al. [1974], Swegle [1990]).

Additional comparison of the Hugoniot data with the curves of earlier workers may be made in Figure 4.3 as well. The curves of McQueen et al. [1963], labeled as A and B, extrapolate well to the present results, while those of Anderson and Kanamori would appear to extrapolate to somewhat denser states than observed. The need to extrapolate, however, weakens any conclusions which might be drawn here.

The waveform observed in experiment ST2 is shown together with several simulations in Figure 4.4. These simulations include the following:

1. The WONDY V simulation with the custom hysteretic release (CHR) used to deduce the release path.
2. A WONDY V simulation with a standard Mie-Grüneisen (MG) model, using Hugo-

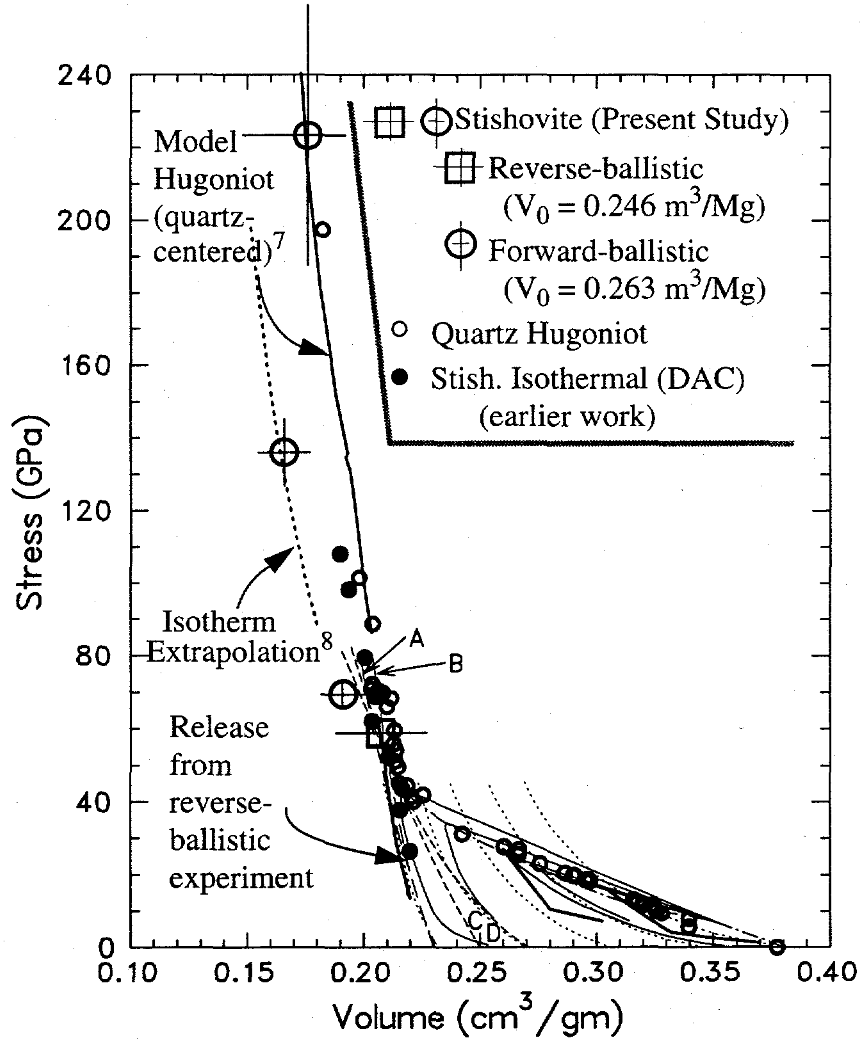

Figure 4.3. Stishovite Hugoniot points from current study plotted with experimental and theoretical curves from Fig. 1.2. Curve "A" is centered at $\rho_0 = 4.3$ gm/cm^3 ($V_0 = 0.233$ cm^3/gm); "B" at 2.65 gm/cm^3 ($V_0 = 0.377$ cm^3/gm) [McQueen et al, 1963]; "C" at 4.0 gm/cm^3 ($V_0 = 0.25$ cm^3/gm); and "D" at 3.7 gm/cm^3 ($V_0 = 0.27$ cm^3/gm) [Anderson and Kanamori, 1968]. Small circles represent an aggregate of previous experiments conducted on quartz; disks are diamond cell data of Tsuchida and Yagi [1989].

niot parameters chosen to exactly fit the interface velocity in the plateau region and a typical Grüneisen gamma ($1.5 \times \rho_0/\rho$). This only differs from (1) in the release properties.

3. A one-dimensional CTH simulation using the same model as (2), to exhibit comparability of results across codes.
4. A two-dimensional CTH simulation using the same model as (2) and (3) to assess the role of edge effects. Model waveforms are shown both for a properly centered velocity sampling point (where the laser spot is focussed, providing input to the VISAR) and for a velocity sampling point 0.5 mm off-center. Since the later does depress the average plateau velocity slightly, it may be concluded that edge effects may cause a too-soft Hugoniot (1 - 2%) to be inferred for a significantly off-center velocity sampling point for the reverse-ballistic geometry. Release curves do not appear to be substantially affected. In the case of greater off-center distances (corresponding to projectile tilt or drift), the apparent release arrival would be earlier, giving a steeper release path in stress/volume space.
5. One- and two-dimensional CTH simulations using the Sesame EOS table generated by PANDA [Kerley, personal communication; see Appendix C]. This is the same Sesame EOS referenced in Figures 4.1 and 4.2, although a starting density of 4.067 gm/cm^3 is chosen because that is correct for this particular test. The Hugoniot state is very slightly softer than calculated from the experimental waveform, although the difference is small. Release properties are comparable to the Mie-Grüneisen releases in the present usage of the Sesame EOS.

Waveforms for the transmitted wave experiments (Series II; tests ST 11 - 13) are unfortunately not available. The push-pull VISAR system was determined shortly after the experiments to not have been properly tuned, and waveform data could not be extracted. (The present experiments were the first to use that VISAR system, and there is wisdom in not using more new components in a setup simultaneously than necessary.) This did not affect our ability to extract arrival timing, from which the present results were deduced.

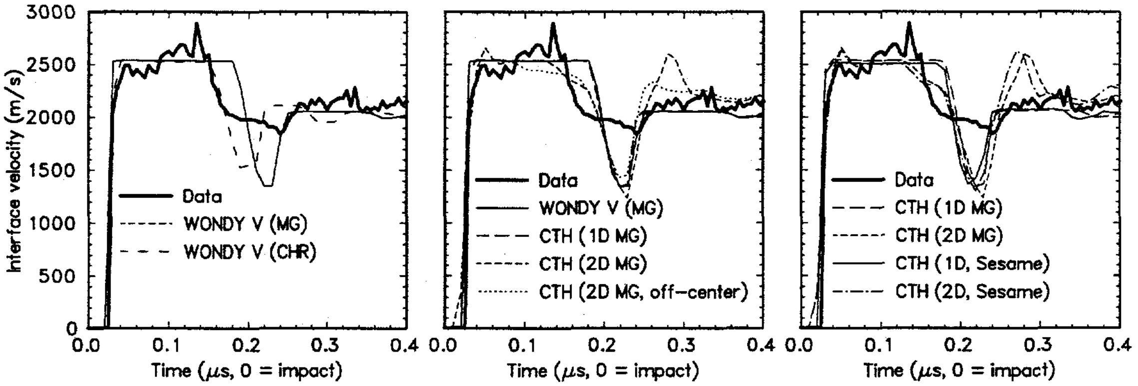

Figure 4.4. Experimental wave profile for test ST2, compared with WONDY and CTH model profiles. MG = Mie-Grüneisen model, CHR = custom hysteretic release model (Section 2.1); Sesame EOS is due to Kerley [personal communication].

Had the waveforms been available for these transmitted-wave experiments, limited release data could have been deduced. The plateau level on the waveform, combined with the sample Hugoniot and the LiF window shock impedance, provides a stress-particle velocity point at approximately 75% of the Hugoniot stress [Furnish, 1993b, pp. 274-5]. Because the path from the Hugoniot point to this partially released point would not be available, the partially released density could not be calculated (its calculation requires a Riemann integration along the release path). Even limited release data would have been interesting and will hopefully be obtained at some time in the <100 GPa region covered by these transmitted wave experiments.

5.0 Summary

Hugoniot data have been obtained for monolithic stishovite over a stress range from < 70 GPa to nearly 180 GPa, using two different experimental configurations. The stishovite samples were of density ~3.9 gm/cm^3 for three of the successful tests and ~4.07 gm/cm^3 for the other one. The data are generally consistent with earlier estimates and modeling. In particular, we see no evidence for a collapse to a high-density (ρ ~ 10 gm/cm^3)

Release data were obtained for one of these experiments (a reverse-ballistic experiment), and are quite consistent with earlier data for quartz-centered experiments.

These data are significant in two respects. First, the Hugoniot data represent a lower-energy locus than had previously been available at high stresses. Second, they show the possibility of obtaining meaningful Hugoniot and wave profiles data from imperfect samples less than 3 mm in diameter.

No evidence is found for a dramatic collapse to densities > 10 gm/cm^3 at stress levels around 125 GPa, as had been suggested by Pavlovskii et al. [1978]; densities at this stress level are about 6 gm/cm^3. At the highest stress levels (~225 GPa), densities are observed to be less than 7 gm/cm^3 (5.8 ± 1.1 gm/cm^3).

References

Anan'in, A. V., O. N. Breusov, A. N. Dremin, S. V. Pershin and V. F. Tatsii, The effect of shock waves on silicon dioxide. I. Quartz., pp. 372-379 in translation of Fizika Goreniya i Vzryva, 10, pp. 426-436, 1974.

Anderson, D. L. and H. Kanamori, Shock wave equations of state for rocks and minerals, *J. Geophys. Res.*, *73*, 6477-6502, 1968.

Barker, L. M. and R. E. Hollenbach, Laser interferometer for measuring high velocities of any reflecting surface, *J. Appl. Phys*, *43*, 4669-4675, 1972.

Boettger, J. C., New model for the shock-induced α-quartz → stishovite phase transition in silica, *J. Appl. Phys.*, *72*, 5500-5508, 1992. Model Hugoniot is good fit to quartz-centered data.

Chhabildas, L. C. and J. M. Miller, Release-adiabat measurements in crystalline quartz, Sandia National Laboratories Report, SAND85-1092, 1985.

Furnish, M. D., Measuring the dynamic compression and release behavior of rocks and grouts associated with HYDROPLUS, Sandia National Laboratories report SAND92-0984, 1993a.

Furnish, M. D., Recent advances in methods for measuring the dynamic response of geologic materials to 100 GPa, *Int. J. Impact Engng.*, **14**, 267-277, 1993b.

Grady, D. E., W. J. Murri and G. R. Fowles, Quartz to stishovite: wave propagation in the mixed phase region, *J. Geophys. Res.*, *79*, 332-338, 1974.

Hemley, R.J., A. P. Jephcoat, H. K. Mao, L. C. Ming and M. H. Manghnani, Pressure-induced amorphization of crystalline silica, Nature, 334, 52-54, 1988.

Hurlbut, C. S. Jr. and C. Klein, Manual of Mineralogy, 19th Ed., p. 414, John Wiley and Sons, 1977.

Kalanin, V. A. and V. L. Pan'kov, Equations of state of stishovite, coesite and quartz, Izv. Earth Physics, No. 8, 1973, pp. 3-16 (translated by M. N. Pillai).

Kerley, G. I., User's manual for PANDA II: A computer code for calculating equations of state, Sandia National Laboratories Report, SAND88-2291, 1988.

Kipp, M. E. and R. J. Lawrence, WONDY V - A one-dimensional finite-difference wave propagation code, Sandia National Laboratories report SAND81-0930, 1982.

Kleeman, J. D. and T. J. Ahrens, Shock-induced transition of quartz to stishovite, *J. Geophys. Res.*, *78*, 5954-5960, 1973.

McQueen, R. G., J. N. Fritz and S. P. Marsh, On the equation of state of stishovite, *J. Geophys. Res., 68*, 2319-2322, 1963.

Pavlovskii, A. I., N. P. Kolokol'chikov, M. I. Dolotenko and A. I. Bykov, Isentropic compression of quartz by the pressure of a superstrong magnetic field., JETP Letters, 27, pp. 264-266, 1978.

Podurets, M. A., G. V. Simakov and R. F. Trunin, On the phase equilibrium in shock-compressed quartz and on the kinetics of phase transitions, *Izv., Earth Physics, 7*, 1976, 3-11 (translated by Joachim Büchner).

Sato, Y., Pressure-volume relationship of stishovite under hydrostatic conditions, *Earth Planet. Sci. Lett, 34*, 307-312, 1977 (based on hydrostatic data over 0 - 11 GPa range).

Stishov, S. M. and S. V. Popava, A new dense modification of silica, *Geokhimiya, 10*, 837, 1961.

Stöffler, D., Coesite and stishovite in shocked crystalline rocks, *J. Geophys. Res., 76*, 5474-5488, 1971.

Swegle, J. W., Irreversible phase transitions and wave propagation in silicate geological materials, *J. Appl. Phys., 68*, 1563 - 1589, 1990.

Tsuchida, Y. and T. Yagi, A new, post-stishovite high-pressure polymorph of silica, *Nature, 340*, 217-220, 1989.

Trunin, R. F., G. V. Simakov, M. A. Podurets, B. N. Moiseyev and L. V. Popov, Dynamic compressibility of quartz and quartzite at high pressure, *Izv., Earth Physics, 1*, 1970, 13-20 (translated by Joachim Büchner).

Trunin, R. F., G. V. Simakov and M. A. Podurets, Compression of porous quartz by strong shock waves, Acad. Nauk. SSSR, Bulletin, Physics of the Solid Earth 1971, #2, pp. 102-106, 1971.

Tsuneyuki, S., Y. Matsuim H. Aoki and M. Tsukada, New pressure-induced structural transformations in silica obtained by computer simulation, Nature, 339, 209-211. 1989.

Wackerle, J., Shock wave compresson of quartz, *J. Appl. Phys., 33*, 922-937, 1962.

Wise, J. L. and L. C. Chhabildas, Laser interferometer measurements of refractive index in shock-compressed materials, pp. 441-454 in Shock Waves in Condensed Matter, Y. M. Gupta (ed), Plenum, 1985.

Yagi, T., Y. Tsuchida, S. Kusanagi and Y. Fukai, Stabilities of SiO_2 stishovite and $CaSiO_3$ perovskite under lower mantle condition, pp. 699-701 in *High Pressure Research 1990, 5*, W. B. Holzapfel and P. G. Johannsen (eds.), Gordon and Breach Science Publishers, 1990.

Appendix A. Summary of Series I Tests

A.1 Details of Test ST2

The configuration for these reverse-ballistic (sample in projectile) tests is detailed in Section 3; refer to Figure 3.1 for a schematic. The present Appendix presents detailed parameters of the successful test, followed by a brief summary of the other tests conducted.

Parameters for test ST2 are presented in Table A.1. Figure A.1 shows the observed waveforms for both the Projectile Velocity VISAR and the Sample VISAR for this test.

Table A.1. Detailed experimental parameters for test ST2

Quantity (distances in mm; velocities in m/s)	
Sample thickness	0.859
Sample diameter	2.40
Sample density	4.067 gm/cm^3
Aluminum thickness (around sample)	1.016
Aluminum backer thickness	3.252
Aluminum buffer thickness	0.239
Window thickness	19.209
Glue bond thickness (buffer/window)	0.022
Projectile velocity	4006
VPF (Sample)	1019.23
VPF (Projectile velocity)	431.16

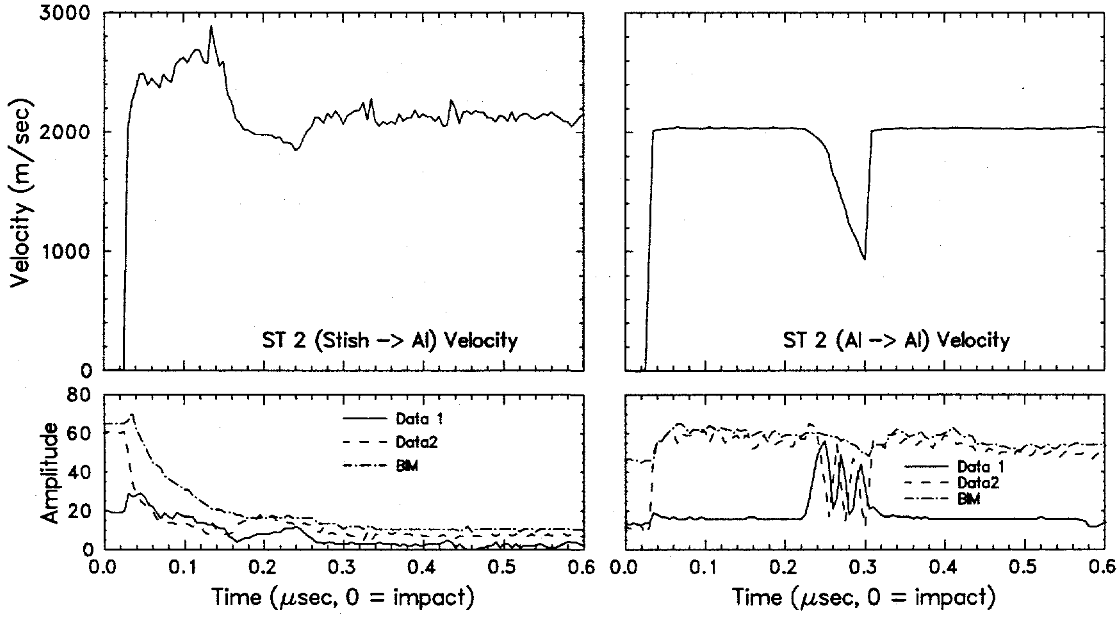

Figure A.1. Velocity profiles and fringe records for Test ST2 (projectile velocity and sample VISARs).

The data from each test of this configuration is comprised of two velocity profiles, one from the Sample VISAR and the other from the Projectile Velocity (aluminum/aluminum) VISAR. Recall that the important quantity from each of these profiles is the level of the *initial plateau*, labeled as "Input to..." in Figure 3.1.

Each velocity profile has an abrupt "step" at the time of first arrival. The rapid acceleration at this point causes several fringes (sinusoidal cycles in the fringe record) to pass too rapidly for the instrumentation to resolve. Hence it is necessary to add an integer multiple of the velocity-per-fringe (VPF) constant to the profile at all times later than the initial arrival. The experiments were designed with sufficiently large VPF values that only one integer choice is reasonable for the jump. For test ST2, 2 VPF constants were added for the sample VISAR and 5 for the projectile velocity VISAR.

In general, the projectile velocity may be estimated to within several (5 - 10) percent from gun loading conditions; as long as the number of VPF constants added for the Projectile Velocity VISAR is not more that about 5, that number of VPF constants may be considered unambiguous.

The proper number of fringes added for the Sample VISAR waveform is determined on the basis of what is physically reasonable. Had 3 VPF constants been added, a shock velocity of 48 km/s would have resulted, while adding only 1 VPF constant would have given a Hugoniot density of 30 gm/cm^3.

Uncertainties in the Hugoniot conditions are calculated be estimating uncertainties in the plateau velocity for the Sample VISAR profiles, in the projectile velocity (via the Projectile Velocity VISAR profiles) and in the sample density (take as 7.5%, reflecting primarily uncertainties in weight and diameter measurements). These are propagated in quadrature to give uncertainties in the Hugoniot quantities. The results are shown in Table 4.2.

As mentioned in the main text, release paths are calculated by modeling the waveform with the Lagrangian wavecode WONDY V, using the method outlined in Section 3. Uncertainties in the release paths are more difficult to quantify than for the Hugoniot state. Parametric analyses of this method of determining release paths have been conducted [Furnish, 1993a,b] for experiments with somewhat larger samples. The primary errors which would contribute to overall uncertainty here are:

- The observed velocity history is qualitatively imperfect; the release arrival is more difficult to define unambiguously than those observed in earlier geomaterial tests [e.g. Furnish, 1993a,b].
- The sample densities are measured less accurately (~7% vs. <1% for examples in Furnish [1993a,b]).
- Thickness is measured less accurately (1 - 2%, vs. 0.2%)
- Edge effects may influence the present profiles after ~100 nsec. In the present case this is probably not a problem, however. Such edge effects would be expected to cause an earlier onset of decreasing velocity in the observed waveform; this would be interpreted as an erroneously steep release in P/ρ or stress/strain space.

A.2 Overview of Series I tests

A variety of tests were conducted in preparation for the tests utilizing the stishovite samples, primarily to provide some assurance that tests using the hard-to-replace stishovite samples would not fail. A matrix in shown in Table A.1. In addition, known test samples (sapphire, copper) were chosen to give some indication of how well data from this configuration could reproduce known material properties. As well, sapphire was expected to show similar shock velocities and densities to stishovite.

The first four tests yielded waveforms which were very difficult to interpret, as well as unreliable indications of impact tilt. A decision was made to halt the series and attempt to resolve any experimental difficulties. Another team had difficulty as well, and the difficulties were traced to a non-straight barrel. Following replacement of the barrel the final five tests were conducted.

Table A.2. Summary of tests conducted in Series I.

Shot	Impact	Sample		VISAR[1]	Tilt	Comments
#	Vel. k/s		Sample	Alum.	mr	
ST-5	4.5	Al_2O_3	P	P	90-100	Projectile velocity VISAR not good
ST-6	4.5	Al_2O_3	P	P	25-30	Tilt from 2 pins only
ST-7	4.5	Cu (Al backer)	P	n.a.	42	Tilt from 4 pins Free-flight; used MAVIS Light lost ~ immediately
ST-1[2]	2.8	Stishovite	P	FB	93	Sample VISAR lost light almost immediately
ST-9	~4.5	Copper	P 1.0192	FB 0.43116		Projectile velocity VISAR at zero intensity
ST-2	3.9	Stishovite	P 1.0192	FB 0.43116		Good data
ST-3	5.3	Stishovite	P 1.0192	FB 0.7691		Missed sample entirely (2 clean Al/Al impact waveforms)
ST-4	~6.8	Stishovite	P 1.0192	FB 0.7691		No clear profiles (severe noise problems)

---

1. P = probe, n.a. means no VISAR used (MAVIS measured projectile velocity), FB means free beam
2. Number 1 assigned because this was the first test with a stishovite sample

Of the final five tests, the cause of failure of the first (ST1) is unclear (possibly related to viewing an edge with the Sample VISAR). The second yielded a good Sample VISAR trace, but no Projectile Velocity VISAR trace (light loss). The third (ST2) produced good data. ST3 gave good waveforms, but analysis showed them to both correspond to aluminum on aluminum impacts, implying that the sample did not impact at the Sample VISAR point. The cause of failure of the final test (ST-9) was unclear, except that a low signal to noise ratio did not allow clear data to be obtained.

Appendix B. Series II Tests

B.1 Transit time measurements

Details of the process of measuring shock transit times in the stishovite samples for the Series II tests are presented here. For a broader discussion of Series II, refer to Section 4.

A schematic of the instrumentation is presented in Figure B.1.

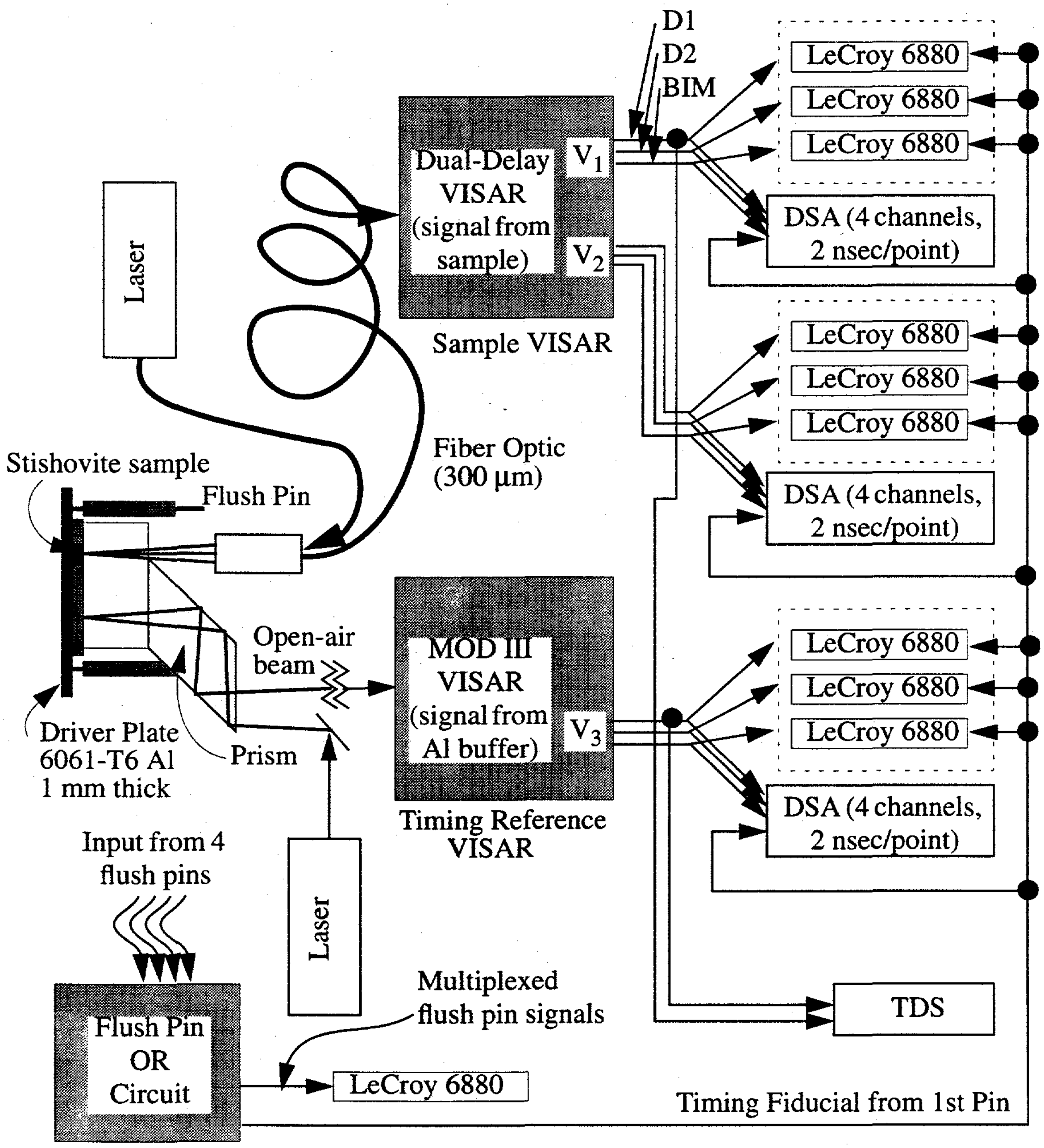

Figure B.1. Schematic of data acquisition system for Series II experiments. DSA, TDS and LeCroy 6880 are digitizers; see text for details.

Interferometer fringe traces from the two VISAR systems were recorded on electronic digitizers, together with timing fiducials. Each set of fringes was recorded on two sets of digitizers, allowing some ability to assess reading errors. The LeCroy digitizers recorded at 0.742 ns/point, with a 500 MHz bandwidth, and were set to add the data and fiducial input channels to produce one trace. The DSA digitizers recorded 4 channels simultaneously in lockstep, with 2 ns/point and an effective resolution of 250 MHz/channel. In addition, Data1 (D1) traces from the two VISAR systems were recorded on a Tektronix TDS system with two lockstep channels, allowing a fiducial-independent check on relative timing of the two traces.

All data and fiducial travel times were carefully measured, including wire, light beam, fiber optic, intra-VISAR travel times and photomultiplier response times. Important travel times are listed in Table B.1 for purposes of illustrating the present procedure.

Table B.1. Timing information for Series II setup[1]

Data travel times for Sample VISAR

	Leg V1	V1 & V2	Leg V2
* Sample to VISAR (61' of 300 μm glass fiber):		92.075 ns	
* Light path within VISAR (57", 66" for V1, V2):	4.83 ns		5.59 ns
* Photomultiplier tube response	14.0 ns		14.0 ns
* Cable to amp + amp response:	7.62 ns		7.28 ns
Cable from amp (V1 Data1) to TDS scope	253.8699 ns		
Cables from amp to DSA digitizers:			
Data1	262.632 ns		252.104 ns
Data2	247.980 ns		246.472 ns
BIM		260.760 ns	
Cables from amp to LeCroy digitizers:			
Data1	269.623 ns		259.225 ns
Data2	254.910 ns		253.463 ns
BIM		270.160 ns	

Data travel times for Timing VISAR

* Sample to VISAR: (49'10" free beam)	50.66 ns
* Within VISAR: (87" path)	7.37 ns
* Photomultiplier tube (PMT) response	14.0 ns
Cable from PMT (Data1) to TDS scope	194.736 ns
Cables from PMT to digitizers:	

	DSAs (Tek 602A)	LeCroy 6880
BIM	189.62 ns	194.16 ns
Data1	203.95 ns	207.04 ns
Data2	187.03 ns	192.03 ns

Fiducial travel times

	DSAs (Tek 602A)	LeCroy 6880
Fid (V1):	3317.969 ns	3317.976 ns
Fid (V3)	3281.57 ns	3277.00 ns

---

[1] Times denoted by asterisks apply to all travel times in category; others are parallel

The first step in calculating the sample shock transit time is to calculate the time of shock arrival for the Sample VISAR relative to that for the Timing VISAR (t_S-t_R), using fiducials and accounting for relative signal travel (transmission) times. This procedure is illustrated in Figure B.2. The objective of this step is to write (t_S-t_R) in terms of the observables (the four T quantities, i.e. the fiducial and shock arrival positions on the digitizer traces; and the signal transit timings Δt). The following equation applies:

$$t_S\text{-}t_R = (T_{S(Arr)}\text{-}T_{R(Arr)}) + (\Delta t_{S(Fid)}\text{-}\Delta t_{R(Fid)}) + (T_{R(Fid)}\text{-}T_{S(Fid)}) + (\Delta t_{R(Arr)}\text{-}\Delta t_{S(Arr)}) \qquad \text{(Eq. B.1)}$$

Fiducials and triggers are generated by the first tilt pin to fire (see bottom of Fig. B.1).

The second step in calculating the sample shock transit time is to calculate the shock transit time through the aluminum ring (see Fig. 4.2), $t_{Al\ Ring}$, using an impedance-match cal-

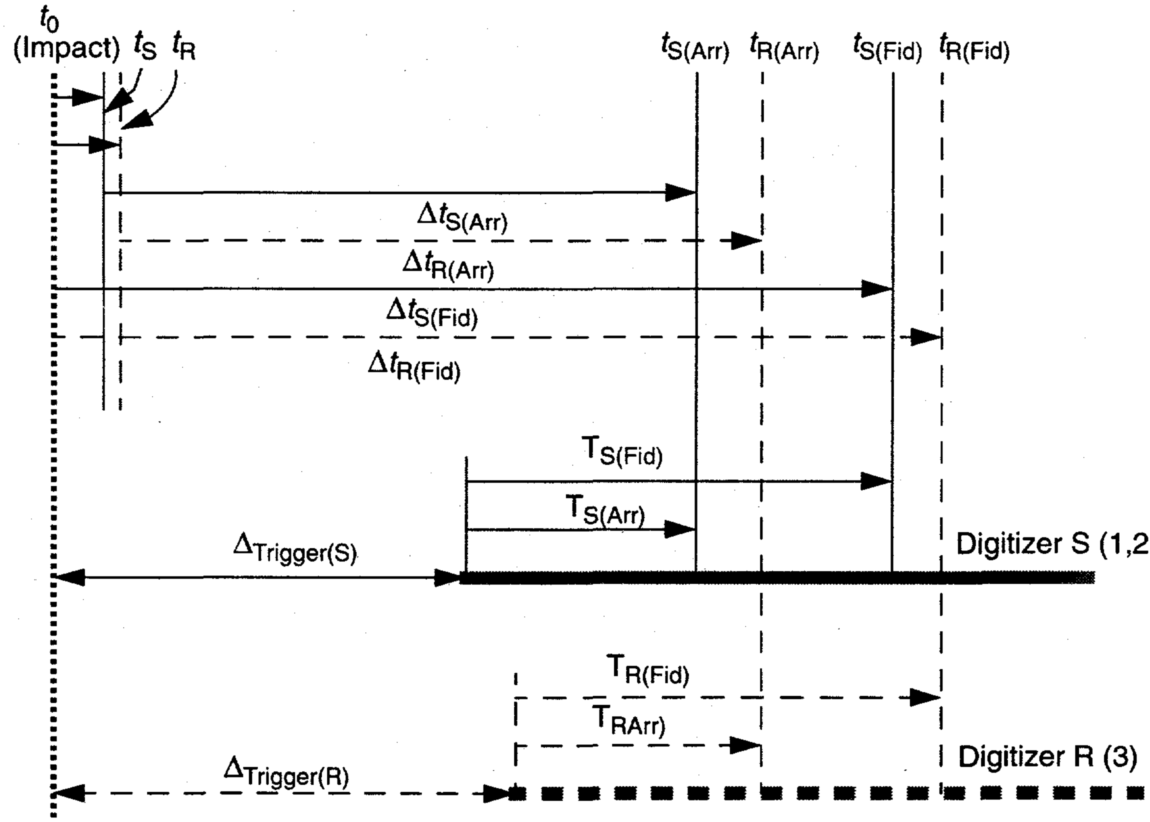

Observables: T (positions in digitizer records for arrival and fiducial)
Δt (transit times through cabling, VISARs)

Goal: Write t_S-t_R in terms of the observables

Figure B.2. Timing diagram for Series II experiments. S refers to sample, R refers to reference, t refers to "absolute" time, T refers to time read from digitizer traces, Δt refers to signal transit times. Dashed lines pertain to traces and data from the Timing (reference) VISAR; solid lines pertain to traces and data from the Sample VISAR.

culation. The result is added to (t_S-t_R) to arrive at the interval between the shock entry into the aluminum ring and its arrival at the sample/window interface.

The final step in calculating the sample shock transit time is to assess the effect of impact tilt. A finite tilt may cause the closure times between projectile and target to differ at the locations monitored by the two interferometers.

Tilt of the impact was assessed by a set of 4 rear-surface tilt pins (coaxial, self-shorting), complemented by 2 additional pins. The first of these pins to fire was also used to trigger the digitizers and generate the timing fiducial. The signatures of the four pins were multiplexed and recorded on a LeCroy 6880 digitizer. For the particular circuitry used, the signature of each pin was a peak of characteristic voltage, with a time offset to prevent overlap. The time offset for each pin was a constant of the circuit and was measured prior to each shot by introducing a test short and recording the output signature. Subtracting off this pin-by-pin time offset gave a set of pin shorting times $t_{FP1..4}$ with correct relative time (i.e. they would all be equal for a "pancake" impact). The arrangement of these pins is shown in Figure B.3. Pins 5 and 6 were monitored on separate digitizers, with a time fiducial to allow correlation

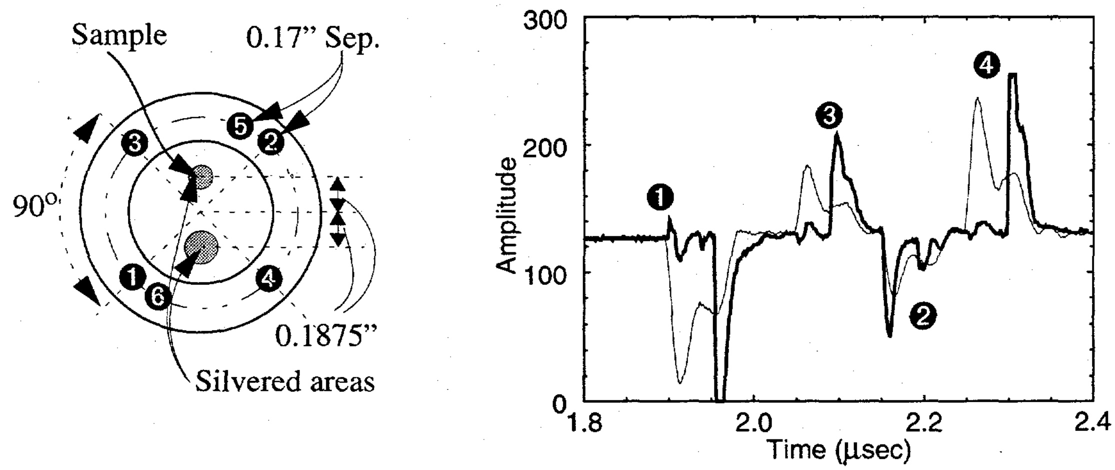

Figure B.3. Flush pin layout and sample spectrum. Bold curve is the calibration curve (analogous to "pancake" impact); fine curve is curve for test ST-12.

We assume the impact is planar, calculating the quantity:

$$t_{Nonplanar} \equiv t_{FP1} + t_{FP2} - t_{FP3} - t_{FP4} \qquad \text{(Eq. B.2)}$$

as a check. This serves as well to flag tests where a pin may have prefired or fired anomalously late.

The additive correction to the stishovite transit time due to impact tilt is then:

$$t_{Tilt} = 0.5 \times (t_{FP1} + t_{FP3} - t_{FP2} - t_{FP4}) \times S/(\sqrt{2}R_{BC}) \qquad \text{(Eq. B.3)}$$

(where S = 9.525 mm is the separation between the two points monitored by VISAR and R_{BC} = 12.065 mm is the bolt circle radius of the tilt pins).

The shock transit time through the stishovite is then written as:

$$t_{\mathrm{Stish}} = t_{\mathrm{Al\ Ring}} + (t_{\mathrm{S}}-t_{\mathrm{R}}) + t_{\mathrm{Tilt}}. \qquad \text{(Eq. B.4)}$$

B.2 Application to Series II tests

The application of the above reduction scheme to the actual data posed a few difficulties; their discussion is the goal of this section.

The way initial arrivals were read deserves comment. For the Timing VISAR (V3), the Data 1 trace (D1) generally lagged Data 2 (D2) and Beam Intensity (BI) by ~15 ns. This is consistent with the signal transmission timings reported in Table B.1. The arrivals read corresponded to the D2 arrival time, and wire timings used were those for D2 throughout. In some cases, D2 did not show a clean breakaway due to the particular fringe phases; D1 was used to infer where the D2 breakaway should be. This is illustrated in Figure B.4.

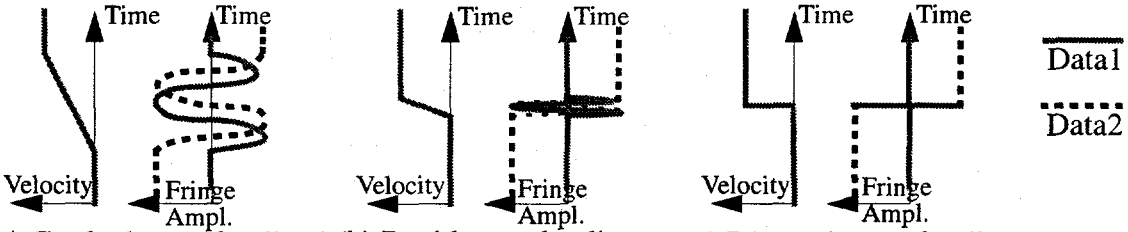

(a) Gradual ramp loading (b) Rapid ramp loading (c) Discontinuous loading

Figure B.4. Illustration of fringe phase in determining breakaway readability. In (a) all fringes are readable. In (c) only Data2 shows jump signature. (b) is intermediate

In general, calculations of (t_S-t_R) (the difference in arrival times of the shock at the two points monitored by VISAR) were made using input from the LeCroys, the DSAs and the TDS digitizers. The option was available of discarding input from 1 - 2 of these sets if the appearance of the data warranted it. On test ST-13, for example, it was extremely difficult to read the Sample VISAR breakaway from the TDS waveforms, and the decision was made to discard the TDS data for that test. The interval (t_S-t_R) varied for a given shot depending on which sets of digitizers were used. Table B.2 shows representative scatter

Table B.2. Summary of time-of-arrival (t_S-t_R) differences deduced from various diagnostics.

(All times in μs)

Test	TDS	DSA	LeCroy	Variation	Variation without TDS
ST-10	---	1.3232	1.3166	0.0066	0.0066
ST-11	0.0129	0.0168	0.0136	0.0039	0.0032
ST-12	-0.0166	-0.0058	-0.0104	0.0108	0.0046
ST-13	---	0.0057	0.0031	0.0026	0.0026
ST-14	0.0489	0.0527	0.0486	0.0041	0.0041
ST-15	0.0529	-----	0.0691	0.0162	----

observed among the digitizing systems. All digitizers were retained in the analysis where possible, with error estimates including the effects of scatter amongst the different digitizer systems.

In certain cases (ST-10 and ST-11), the tilt pin data did not make sense unless the last pin to fire was discarded. More specifics are discussed below. For test ST-14 (copper sample), Pin #2 did not fire, so no pins could be discarded without leaving the tilt undefined. In that particular instance, a large tilt (corresponding to a 60 ns difference in impact times at the sample and Timing VISAR sites) was indicated; it is likely a more realistic tilt would have been registered had Pin#2 fired and one of the other pins been discarded.

Originally the "dummy" tests ST-14 and ST-15 (copper samples) had been proposed as checks on the timing calibration. Two problems arose with this. First, the time fiducial wiring was changed after these tests and before the stishovite tests ST-10 - ST-13. The fiducial wiring for the stishovite tests is as shown in Figure B.1. By contrast, the wiring for the dummy tests used an optical fiducial; i.e. the output of the OR circuit was fed to LED's in the VISARs, which placed a pulse over the late-time data. Hence these tests could not be used with confidence as timing calibrations. Second, there were significant inconsistencies between the transit times inferred for the two tests. An 80 nsec variation was observed, with ST-15 having the longer transit time, although the transit times should have been comparable. The difference appears to be primarily due to poorly controlled tilt on ST-14; Pin #2 was not recorded and the remaining 3 pins gave a high tilt. These tests were not given further consideration.

Specific comments about the individual tests follow. The tests are ordered chronologically.

- Test ST-15 (copper sample): There was no DSA reading on the Timing VISAR, and the difference in (t_S-t_R) calculated from the LeCroy digitizer and from the TDS digitizer was 15.8 ns (which is substantial). Optical fiducial used (affected all scopes).
- Test ST-14 (copper sample): Tilt Pin 2 did not fire on this test, so no variations in the analysis involving excluding flush pins could be conducted. (t_S-t_R) values calculated from the various digitizer systems were in good agreement. The transit was expected to be about 13 ns more than for ST-15, while it was calculated to be 75 ns less (most likely due to tilt issues). Optical fiducial used (affected all scopes).
- Test ST-10 (stishovite sample): The interval (t_S-t_R) is calculated as ~1.3 μsec, which is far too large to make sense. No obvious cause is available. Tilt Pin 4 appears to have fired late by 136 ns, and was excluded from the analysis.
- Test ST-11 (stishovite sample): Pin 4 apparently fired late (~210 ns). Eliminating this from the calculations gives a sensible result.
- Test ST-12 (stishovite sample): The results from the LeCroy and DSA digitizer systems were sensible. The TDS digitizer gave a much shorter transit time than did the other diagnostics (~8 nsec shorter than the LeCroys and 12 nsec shorter than the DSAs) and was excluded from the analysis.

- Test ST-13 (stishovite sample): Although the tilt pins did not give a clean planar signature, none could be readily excluded as obviously late. An analysis of the records from Pins 5 and 6 did not clarify the question; Pin 5 appears to have fired 4.085 µs before Pin 6. The nonplanarity recorded was about 70 ns. At the impact velocity used for this test (6.54 km/s), impactor distortion is not unusual. The large uncertainty reported for this point includes the effect of this nonplanarity.

B.3 Series II test experimental parameters

The matrix of tests conducted is summarized in Table B.3. Four tests were conducted with stishovite samples, while two preliminary tests were conducted using copper samples (OHFC Cu). Testing progressed in the order ST-15, 14, 11, 12, 13, and 10.

The tests with copper samples were intended to provide a check on the system timing and reproducibility. The stishovite tests followed the copper tests. Unfortunately, an inadvertent wiring switch defeated this check (see previous section) and the copper test results were not used.

Table B.3. Test matrix for Series II experiments

Test	ST-10	ST-11	ST-12	ST-13	ST-14	ST-15
Proj. Vel. (km/s)	3.1507	4.8782	4.9786	6.5357	4.8532	4.9062
Sample measurements -						
Machined Thick (mm)	1.003	0.998	0.997	0.999	1.056	1.035
Final Lapped Thick (mm)	0.846	0.931	0.978	0.977	1.054	0.976
Diameter (mm)	3.913	3.600	3.700	3.872	3.721	3.70
Density (gm/cm^3)	3.822	3.959	3.954	3.833	8.93	8.93
Label	ST-10	ST-11	ST-12	ST-13	Cu	Cu
Impactor Mat'l/Thick	Al/2.998	Al/2/995	Ta/1.030	Ta/0.779	Al/2.987	Al/2.975
Al Driver Thick (mm)	1.033	1.037	1.035	1.008	1.021	1.03
Al Ring Thick (Sample)	0.846	0.931	0.975	0.977	1.054	0.976
Al Ring Thick (Timing)	0.845	0.930	0.980	0.977	1.059	0.976
Velocities-per-Fringe (km/s)						
VPF Sample (1)	0.410	0.410	0.800	0.800	0.410	0.410
VPF Sample (2)	0.305	0.564	0.564	1.096	0.564	0.564
VPF Timing	0.431	0.431	0.431	0.431	0.431	0.431
Glue Bond Thicknesses (mm)						
Driver/Sample	0.006	0.003	0.000	0.006	0.011	0.000
Sample/Window	Not Rec.	0.000	0.000	0.005	0.006	0.006

Appendix C. PANDA input deck for Sesame EOS

The following input deck for the PANDA II program [Kerley, 1988] supplies the equation of state referenced in Section 4 for stishovite-centered shock loading.

Kerley [personal communication] emphasizes that this EOS is preliminary, unpublished and incomplete; the phase transition has been addressed only in exploratory calculations and no attempt has been made to build in a reverse transition. PANDA is capable of handling more sophisticated EOS descriptions; the reader is referred to Kerley's earlier work on $CaCO_3$[1] as an example. We are grateful that he has allowed us to reference this EOS in the present work.

```
!***********************************************************************
!
!  01/05/94 - EOS for stishovite SiO2.
!  See GIK Notebook 26-65.
!  Tabular cold curve is computed from Birch-Murnaghan expression with
!    R0=4.30, B0=350., B0P=3.8. R0 matches RT density, B0 matches data
!    of Liu, Bassett, and Takahashi, B0P gives smooth extrapolation to
!    TFD limit and is agrees fairly well with data of Tsuchida & Yagi.
!  Thermal nuclear terms chosen to match data of Holm et. al..
!  Parameter ESFT is chosen so that energy at RTP is equal to heat of
!    transition from quartz to stishovite (0.822 MJ/kg).
!
!***********************************************************************
mod sol crv=1 nuc=1 vrt=1 esft=0.64686
si[1]o[2]
10 4.285 298 2.0 555
4 8 4.25 1
tty
4.0000E+00 -2.2060E+01
4.2500E+00 -4.0037E+00
4.5000E+00  1.7347E+01
4.7500E+00  4.2078E+01
5.0000E+00  7.0271E+01
5.2500E+00  1.0200E+02
5.5000E+00  1.3732E+02
5.7500E+00  1.7631E+02
6.0000E+00  2.1900E+02
6.2500E+00  2.6546E+02
6.5000E+00  3.1573E+02
```

---

[1] G. I. Kerley, Equations of state for calcite minerals. I. Theoretical model for dry calcium carbonate. High Pressure REsearch, 2, 29-47, 1989. Also see G. I. Kerley, Theory of calcite equation of state, pp. 613-616 in Shock Compression of Condensed Matter - 1989, S. C. Schmidt, J. N. Johnson and L. w. Davison (eds.), Elsevier, 1990.

```
6.7500E+00  3.6984E+02
7.0000E+00  4.2783E+02
7.2500E+00  4.8974E+02
7.5000E+00  5.5560E+02
7.7500E+00  6.2542E+02
8.0000E+00  6.9924E+02
8.2500E+00  7.7707E+02
8.5000E+00  8.5892E+02
0 0
-1 2
- - - 2
650 4 100
800 2 100

isob sol 0 298 0 1 4.3
isob sol 0 50 300 6 4.3
eos sol
4.2847 298

mod sol nuc=0 vrt=0
plot crvthy
isot sol 4.31 6 25 1 0 0 1 1
Calculated cold curve for stishovite
isot sol 6 50 50 2 0 0 1 1

mod sol nuc=1 vrt=1
plot hugthy
hug sol 4.297 0 0 70 6000 60
Calculated Hugoniot for stishovite, shocked from RZRO=4.297
hug sol 3.900 0 0 120 7000 60
Calculated Hugoniot for stishovite, shocked from RZRO=3.90
hug sol 2.650 0 0 1000 12000 60
Calculated Hugoniot for stishovite, shocked from RZRO=2.65
hug sol 2.204 0 0 500 9000 60
Calculated Hugoniot for stishovite, shocked from RZRO=2.204
hug sol 2.145 0 0 500 9000 60
Calculated Hugoniot for stishovite, shocked from RZRO=2.145
hug sol 1.877 0 0 500 9000 60
Calculated Hugoniot for stishovite, shocked from RZRO=1.877
!  Make table for use in phase transition model
mesh sol
3.5 4.2847 5 1
4.2970 8.9 16 3 298   ! 16 points from 1 to 1000 GPa
0 0 0 0
10 298 5 1
298 1.e4 35 2
```

```
0 0 0 0
slib sol
301
no
201
30,60.0843,0.0,298,4.2847
0
403 010594 b403 a403
end
```

Distribution

External Distribution:

University of Washington
Geophysics Program
Box 351650
Seattle, WA 98195-1650
Attn: J. Michael Brown

California Research and Technology
20943 Devonshire St.
Chatsworth, CA 91311-2376
Attn:
Anne Cooper
Sheldon Schuster

CEWES-SD
Waterways Experiment Station
3909 Halls Ferry Road
Vicksburg, MS 39180
Attn:
Ed Jackson
Joe Zelasko

DNA Nevada Operations Office
P.O. Box 98539
Las Vegas, NV 89193-8539
Attn:
Barbara Harris-West

FCDNA/FCTTS
1680 Texas St SE
Kirtland AFB, NM 87117
Attn:
George Baladi, FCTTS
Mike O'Brien, FCTO
George Lu, FCTI
Audrey Martinez, FCTTS
Eric Rinehart, FCTTS
Bob Reinke, FCTTS
Byron Rystvit, FCTTS

HQ/DNA DFTD
6801 Telegraph Road
Alexandria, VA 22310-3389
Attn:
Don Linger, Fran Rensvold

Ktech Corp
901 Pennsylvania Ave NE
Albuquerque NM 87110
Attn:
Frank Davies
Eric Smith
Larry Lee

Lawrence Livermore National Laboratory
P.O. Box 808
Livermore, CA 94550
Attn:
Armand Attia, Mail Stop L-200
Dave Erskine, Mail Stop L-417
Lewis Glenn, Mail Stop L-200
Bill Moran, Mail Stop L-200
Kurt Sinz, Mail Stop L-200

Los Alamos National Laboratory
Los Alamos. NM 87545
Attn:
Arthur Cox, T-6 M/S B268
Thomas Dey, EES-5 M/S F665
James D. Johnson, T-1 M/S B221
James N. Johnson, T-1 M/S B221

R&D Associates
P.O. Box 9377
Albuquerque, NM 87119
Attn:
Larry Germain
Barbara Killian

SAIC/Pacifica Technology
10260 Campus Point Drive, MS 62
San Diego, CA 92121
Attn:
Martin Fogel
Dan Patch
Mike McKay
Jack Klump

S-Cubed, A Division of Maxwell
Laboratories, Inc.
3398 Carmel Mountain Road
San Diego, CA 92121
Attn:
Jim Baker
Steve Peyton

S-Cubed, A Division of Maxwell
Laboratories, Inc.
P.O. Box 1620
San Diego, CA 92038-1610
Attn:
Phil Coleman
Norton Rimer

Robert Bass
4505 Durango Ct. NE
Albuquerque, NM 87109

SRI International
333 Ravenswood Ave.
Menlo Park, CA 94025
Attn:
Don Curran
Paul deCarli

Thomas J. Ahrens
Seismological Laboratory
Division of Geological and Planetary
Sciences
California Institute of Technology
Pasadena, CA 91125

Tom Duffy
Carnegie Institution of Washington
Geophysical Laboratory
5251 Broad Brach Road, NW
Washington, D. C. 20015-1305

Conrad Felice
Dames & Moore
500 Market Place Tower
2025 First Avenue
Seattle WA 98121

Kerley Publishing Services
P.O. Box 13825
Albuquerque NM 87192
Attn: Gerald Kerley

Paul Fisher
Springfield Research Facility
P.O. Box 1220
Springfield, VA 22151

Edward S. Gaffney
GRE Corp
2921 Carlisle Blvd NE
P.O. Box 30863
Albuquerque NM 87190-0863

Yogi. M.Gupta
Dept. of Physics
Shock Dynamics Laboratory
Washington State University
Pullman, WA 99124-2814

Skip Knowles
JAYCOR
1608 Spring Hill Road
Vienna, VA 22182-2270

Wesley Martin
Terra Tek
420 Wakara Way
Salt Lake City, Utah 84108

Frank McMullen
Tech Reps
5000 Marble Ave NE
Albuquerque NM 87110-6390

John L. Remo
Quantametrics, Inc.
#1 Brackenwood Path
Head of the Harbor
St. James, NY 11780

Ken Sites
SAIC
P.O. Box 19057
Las Vegas, NV 89119

Tsutomo Mashimo
Kumamoto University
Kurokami 2-39-1
Kumamoto 860
JAPAN

Dr. Hidiyuki Fujisawa (3)
Earthquake Research Institute
The University of Tokyo
No. 1-1, Yayoi 1-chome, Bunkyo-Ku
Tokyo 113
JAPAN

Dr. Eichi Ito (3)
Institute for Study of Earth's Interior
827, Yamada, Misasa-cho
Tohaku-gun, Totori 682-01
Okayama 700
JAPAN

Sandia Internal Distribution:

MS 0321	1400	E. H. Barsis
MS 1111	1402	S. J. Dosanjh
MS 1110	1404	J. A. Ang
MS 0318	1415	G. S. Davidson
MS 1111	1421	S. Dosanjh
MS 1110	1422	R. C. Allen
MS 1110	1423	Manager
MS 1109	1424	A. L. Hale
MS 0441	1425	P. L. Stanton
MS 0819	1431	J. M. McGlaun
MS 0820	1432	A. Farnsworth
MS 0820	1432	M. E. Kipp
MS 0820	1432	F. R. Norwood
MS 0820	1432	P. Yarrington
MS 0821	1433	L. C. Chhabildas
MS 0821	1433	D. Crawford
MS 0821	1433	M. D. Furnish (20)
MS 0821	1433	D. E. Grady
MS 0439	1434	D. R. Martinez
MS 0437	1518	J. B. Aidun
MS 0437	1562	E. P. Chen
MS 1454	2554	L. J. Weirick
MS 0427	5101	R. McIntosh
MS 0458	5602	J. R. Asay
MS 1033	6111	J. L. Wise
MS 0751	6117	W. R. Wawersik
MS 0899	13414	Technical Library (5)
MS 0619	12615	Print Media
MS0100	7613-2	Document processing for DOE-OSTI (2)
MS 9018	8523-2	Central Technical Files
MS 1159	9311	T. K. Bergstresser
MS 1159	9311	L. Hill
MS 1159	9311	C. Smith
MS 0355	9723	M. J. Forrestal